Meso-scale response of concrete under high temperature based on coupled thermo-mechanical and pore-pressure interface modeling

Antonio Caggiano*

CONICET, LMNI, INTECIN, Facultad de Ingeniería, Universidad de Buenos Aires (UBA), C1127AAR, Ciudad Autónoma de Buenos Aires, ARGENTINA

Institut für Werkstoffe im Bauwesen, Technische Universität Darmstadt, Germany

e-mail: acaggiano@fi.uba.ar, caggiano@wib.tu-darmstadt.de

Diego Said Schicchi

Instituto Nacional de Tecnología Industrial, Parque Tecnológico Migueletes, Buenos Aires, ARGENTINA

Stiftung Institut für Werkstofftechnik (IWT), Badgasteiner Str. 3, 28359 Bremen, Germany,

e-mail: dmsaid@inti.gob.ar, schicchi@iwt-bremen.de

Guillermo Etse

CONICET, Universidad Nacional de Tucumán and Universidad de Buenos Aires (UBA), ARGENTINA

e-mail: getse@herrera.unt.edu.ar

Marianela Ripani

LMNI, INTECIN, Facultad de Ingeniería, Universidad de Buenos Aires (UBA), C1127AAR, Ciudad Autónoma de Buenos Aires, ARGENTINA

e-mail: mripani@fi.uba.ar

*Corresponding Author.

ABSTRACT

This work proposes a meso-scale approach for modeling the failure behavior of concrete exposed at elevated temperature inducing thermal damage. The procedure accounts for a thermo-mechanical and pore-pressure based interface constitutive rule. More specifically, the model represents a straightforward extension of a coupled thermo-mechanical fracture energy-based interface formulation, accounting now for damage induced by the temperature dependent pore-pressure effects in concrete. The nonlinear response of the proposed fully coupled interface model for porous cohesive-frictional composites, like concrete, is activated under kinematic, temperature and/or hydraulic increments (with or without jumps). A simplified procedure is proposed to consider the temperature dependent pore-pressure action. After describing the updated version of the interface model, this work focuses on numerical analyses of concrete failure response under high temperature tests. Particularly, meso-scale analyses demonstrate the predictive capabilities of the proposed formulation.

KEYWORDS: Thermal damage, Fracture, Discrete Crack Approach, Meso-scale, Pore-pressure.

1. INTRODUCTION

High temperature in concrete members represents a field of great interest due to its crucial influence in terms of induced thermal damage, affecting strength, durability and serviceability conditions of structural components. Specifically, exposure to high temperature and/or fire represents one of the most destructive events that concrete constructions and structures can suffer [1][2]. The most relevant mechanical properties of concrete and cementitious mortar composites such as cohesion, friction, stiffness and strength show severe degradation under long term exposure to these critical conditions [3][4].

Experimental evidence shows that above 300 ºC, the chemical composition, the micro- and mesoscopic physical compositions, as well as the moisture content (through the inner open porosity) of concrete change drastically [5] [6]. This is due to both the dehydration process of the hardened cement paste and the conversion of calcium hydroxide into calcium oxide [7]. As a consequence, during and after long term exposure to high temperature, the most important mechanical features of concrete such as cohesion, tensile and compressive strengths, Young's modulus and Poisson's ratio show dramatic and radical decreases [8][9].

When temperature rises, particularly in the range 20-200 ºC, cementitious materials quickly diminish their mass per unit volume because of the loss of evaporable water. In the range between 200 and 600 °C the mass loss rate continuously and monotonically decreases. This is mainly due to the loss of water chemically combined to the calcium silicate hydrates. Beyond 600 °C the decomposition of magnesium and calcium carbonates, constituting the concrete matrix, causes further weight loss, which may reach up to 10 % of its original value [10][11][12].

Plenty of the available scientific articles related to experimental studies on concrete deal with the evaluation of its mechanical properties variations when subjected to increasing temperature, with special attention on durability aspects. The study of pore size distribution in concrete exposed to thermal action (up to 800 °C) has been addressed by Janotka and Bagel [13]. This work confirmed

that under increasing temperatures the pore size mainly grows and its distribution becomes more and more homogeneous throughout the concrete bulk. Porosity of concrete subjected to high temperatures may increase up to 40 % of its initial value. It is worth mentioning that porosity's rise is not only due to the evaporable water loss, but also to the dehydration of the gel structure formed by the calcium-silicate hydration products [14].

One of the crucial and most investigated phenomena in concrete components subjected to fire or high temperature is the so-called "spalling effect". Such a phenomenon has been analyzed both, experimentally [15][16] and theoretically [17][18]. Particularly, the process of spalling is quite complex. The literature on this matter underlines that it mainly depends on several coupling actions: i.e., the porosity of the cement matrix, the amount of water content and the stress state either due to thermal gradients and/or applied mechanical loads. During heating, the water within the concrete is transformed into steam and tends to migrate to colder areas of the matrix. Once the vapor flux reaches the coldest zones it condenses again, forming a fully saturated water layer. This process typically occurs in regions of the concrete components located near the heated surface. These regions where this phenomenon develops are commonly called "moisture clog". They are characterized by a low permeability, generating an impermeable barrier to gases flux. Thus, the continuous temperature rise, with the subsequent generation of further vapor gases, which cannot escape to colder areas due to the presence of the water barrier, generates pore-pressure. Such increase in the pore-pressure, added to the stresses induced by thermal strains, mainly activates the spalling mechanism. It is important to remark that pore-pressure mainly acts as a trigger of this mechanism. Once the cracking process starts, and despite the quick pore-pressure release, the spalling mechanism further develops due to the already generated strong localization of failure and the action of increasing thermo-mechanical stresses [19][20].

In this paper the discrete-crack approach is followed to simulate, at the mesoscopic level of observation, the failure behavior of porous materials, such as concrete, when subjected to long term

exposure to high temperature. To this end, a zero-thickness interface constitutive theory for thermo-poroinelastic cementitious composites is formulated, which is based on a further extension of the temperature dependent interface model for non-porous materials by Caggiano and Etse [21]. The proposed interface theory includes a novel pressure-dependent dehydration rule accounting for the porosity features of concrete and thermal conditions. The thermo-poroinelastic interface model, as shown in this work, allows accurate mesoscopic simulations of concrete failure process when subjected to arbitrary combinations of high temperature or fire and mechanical loading.

After the abovementioned brief literature review, Section 2 summarizes the modeling assumptions based on a meso-mechanical approach for the coupled thermo-mechanical problem. In Section 3 the temperature dependent interface theory is formulated, which is used for numerical analyses of cracking behavior of quasi-brittle porous materials such as cementitious mortar and concrete in the framework of the discrete crack approach. Section 4 presents the validation of the proposed interface model. The considered finite element approach for the evaluation of concrete failure processes at the mesoscopic level of observation, under different temperatures and mechanical loading, clearly demonstrates the soundness and capability of the numerical tools. Some concluding remarks are finally drawn out in Section 5.

2. MESOSCOPIC THERMO-MESOMECHANICAL PROBLEM

A mesoscopic procedure for the numerical analysis of concrete specimens subjected to arbitrary combined effects of temperature and mechanical actions is presented in this section. Particularly, concrete is represented as a 2D composite material characterized by large aggregates embedded in a surrounding cementitious matrix (which represents the mortar paste plus fine aggregates).

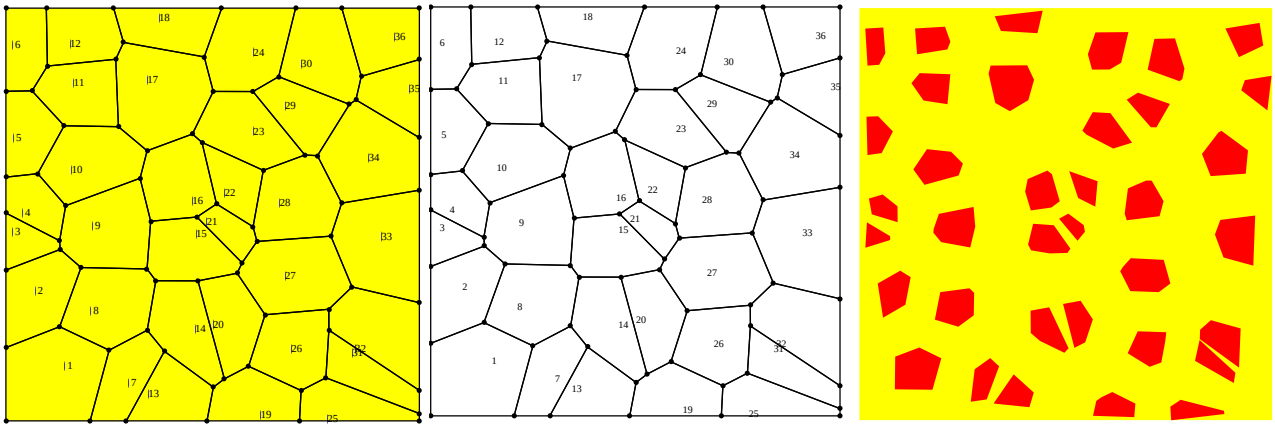

(a) (b) (c)

Figure 1: Concrete meso-structure: (a) randomly perturbed points distribution, (b) Voronoi diagram and (c) explicit meso-geometry.

The meso-scale modeling procedure accounts for the following assumptions:

- A convex polygonal representation is adopted for both large aggregates and the surrounding mortar matrix. They are numerically generated through standard Voronoi/Delaunay tessellation procedure [22] starting from a regularly distributed array of points. These are then slightly perturbed (Figure 1a) with the aim of obtaining the so-called Voronoi diagram (Figure 1b). Once this diagram is obtained the explicit mesoscopic structure can be obtained by resizing and randomly rotating the Voronoi polygons (Figure 1c). It is worth mentioning that the explicit meso-geometry of a concrete specimen can be also obtained by advanced

scanning tomographic procedures, i.e. by means of “CT scan” techniques (computer-processed combinations of X-Ray images), as employed in real specimens [40][41].

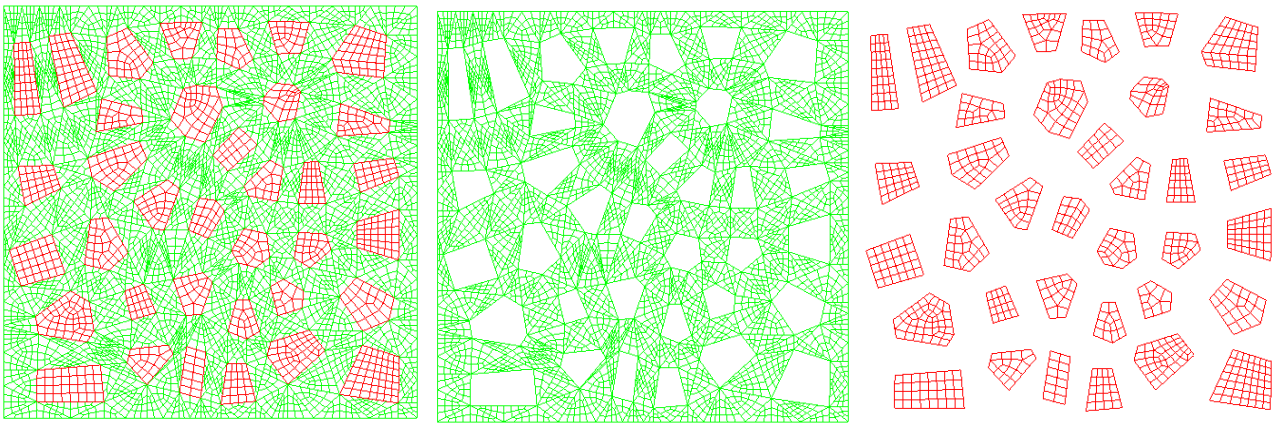

(a) (b) (c)

Figure 2: FE mesoscopic discretization: (a) concrete specimen, (b) surrounding matrix and (c) coarse aggregates [23][24].

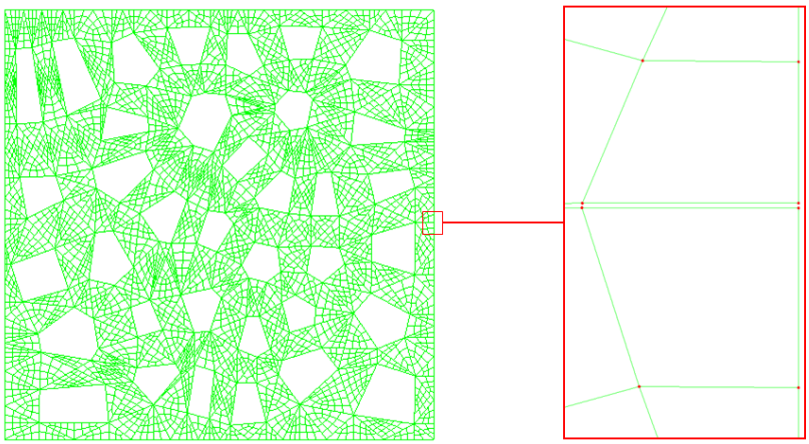

Figure 3: Detail of a zero-thickness interface introduced between two continuous elements.

- 2D Finite Element (FE) mesh is generated through the discretization of each mesoscopic polyhedron particle into iso-parametric 4-nodes elements as schematically indicated in Figure 2. Particularly, thermoelastic finite elements are considered for both aggregate and

mortar continuum elements, being temperature and displacements the node variables. Elastic properties of concrete play a key role in its overall temperature-dependent response. Based on several experimental results [6][25][26] the dependency of the concrete elasticity modulus E and of the Poisson's ratio ν on the temperature rise can be approximated by means of the following temperature-based rules $E = E_0\left(1-\alpha_E\theta\right)$ and $\nu = \nu_0\left(1-\alpha_\nu\theta\right)$, where $\theta = T - T_0$ is the temperature rise (being T and T_0 the actual and reference temperatures, respectively), E_0 and ν_0 are the elastic modulus and Poisson's ratio at a reference temperature T_0, respectively, and lastly α_E and α_ν are degradation parameters to be calibrated (suggested values by the authors for normal strength concrete are $\alpha_E = 0.0014$ and $\alpha_\upsilon = 0.0010$).

- 4-nodes Interface Elements (IEs) are thus introduced along contiguous continuum elements of the matrix material as well as along all joints between aggregates and matrix elements (more details are provided in Section 4, specifically in Figure 20) by means of a proper node duplication and update of the FE connectivity matrix, see Figure 3. The fine mesh discretization of the mesoscopic concrete structure and the inclusion of IEs along all solid element joints, allow to reproduce the most critical cracking mechanism compatible with the (mesoscopic level of observation) boundary conditions of the considered problem.
- Thermomechanical fracture processes in concrete mesoscopic structures are modeled in this work through dissipation mechanisms in the zero-thickness interfaces. They are based on a novel fracture-based model combined with a thermal damage and pore-pressure constitutive law. The complete description of the interface constitutive model is provided in Section 3.

It should be noted that the location of cracks in discontinuous models based on zero-thickness interfaces is pre-defined, since the IEs are "a priori" inserted. This feature of the so-called discrete crack approach, based on fix interfaces, which is used in this paper to model the whole

dissipation and fracture processes taking place in both, aggregate-to-mortar and mortar-to-mortar interfaces, may lead to a strong mesh dependency of the numerical results. However, this mesh dependency of the failure predictions, when based on fix located interfaces, strongly decreases, and their overall objectivity significantly improves, if sufficiently fine meshes or discretizations are considered [42] [43] [44]. In these cases, due to the high density of the involved meshes, the crack grow, in any possible stage of the failure process, may follow the most critical path for reaching the maximum energy dissipation, compatible with the applied displacement excitation.

Lastly, it is worth remarking that the inclusion of interfaces connecting solid mortar elements, instead of modeling the non-linear behavior of this material by means of continuous material formulations, strongly contributes to reduce the mesh dependency of the results associated with the so-called smeared crack approaches.

3. DISCONTINUOUS THERMO-ELASTO-PLASTIC INTERFACE MODEL

This section describes the temperature-dependent interface formulation aimed at analyzing coupled thermomechanical cracking behavior of quasi-brittle porous materials such as cementitious mortars and concretes. The constitutive equations are formulated in terms of effective contact stresses vs. relative displacements, defined at the discontinuity joint mid-plane.

Similarly to Segura and Carol [27], the effective stress vector $\bar{\mathbf{t}} = \left[\bar{\sigma}_N, \sigma_T\right]^T$ on the interface's mid-plane is defined as

$$\bar{\mathbf{t}} = \mathbf{t} + \alpha_j \mathbf{b} p_{vp} \,. \tag{1}$$

where $\bar{\sigma}_N$ and σ_T are the effective normal and total shear components, respectively, α_j the discontinuity Biot's coefficient [27] and, $\mathbf{b} = \left[1, 0\right]^T$ a vector that accounts for the fluid pore-pressure acting in the normal direction to the interface axis. Moreover, $\mathbf{t} = \left[\sigma_N, \sigma_T\right]^T$ is the total interface stress vector, being σ_N the total normal component.

3.1.Fracture/temperature-based model for plain mortar/concrete interface

Fundamental constitutive equations of the thermo-poroplastic interface model are [21]

$$\begin{aligned} \dot{\mathbf{u}} &= \dot{\mathbf{u}}^{el} + \dot{\mathbf{u}}^{cr} + \dot{\mathbf{u}}^{th} \\ \dot{\mathbf{u}}^{el} &= \mathbf{C_d}^{-1} \cdot \dot{\bar{\mathbf{t}}} \\ \dot{\bar{\mathbf{t}}} &= \mathbf{C_d} \cdot \left(\dot{\mathbf{u}} - \dot{\mathbf{u}}^{cr} - \dot{\mathbf{u}}^{th}\right) \end{aligned} \tag{2}$$

where $\dot{\mathbf{u}} = [\dot{u}, \dot{v}]^T$ is the rate of the relative interface displacement vector, additively decomposed into the elastic, plastic and thermal components, $\dot{\mathbf{u}}^{el}$, $\dot{\mathbf{u}}^{cr}$ and $\dot{\mathbf{u}}^{th}$. As previously highlighted $\dot{\bar{\mathbf{t}}} = [\dot{\bar{\sigma}}_N, \dot{\sigma}_T]^T$ is the rate vector of effective stresses and $\mathbf{C_d}$ the thermally degraded elastic stiffness matrix, with k_N and k_T the normal and tangential elastic stiffness, respectively, affected by the scalar damage variable as reported in [21].

The rate of effective normal and tangential interface stresses takes the form

$$\dot{\mathbf{t}} = \mathbf{C_d}^{ep} \cdot \dot{\mathbf{u}} - \bar{\mathbf{f}}[\dot{T}] \tag{3}$$

being $\mathbf{C_d}^{ep}$ the tangential interface stiffness for elastoplastic degradation and $\bar{\mathbf{f}}[\dot{T}]$ the thermal interface effective stresses due to the temperature rate. Further details of the coupled thermo-mechanical interface model formulation can be seen in [21].

3.2. Pore-pressure description

Classical procedures for modeling drying and vapor diffusion phenomena in porous media like concrete follow the calculation of moisture diffusion processes. Particularly, plenty of models account for simulating the migration (flux) of the "evaporable water" throughout the pore structure of cementitious composites through diffusion-type approaches [28]. Thereafter, the pore-pressure can be computed from the combined effect of moisture diffusion and temperature rising phenomena coupled with thermally dependent mechanical effects.

The moisture diffusion, which is a quite complex phenomenon in concrete computational mechanics, and more specifically within the framework of the coupled thermomechanical interface model formulation outlined in this work, is here not taken into account. The emphasis of the proposed interface model formulation is the analysis of porous media like concrete when subjected to the combined action of mechanical loading and high temperature in the spirit of a fully coupled numerical tool. Nevertheless, this formulation accounts for porous media features of concrete, allowing to explicitly consider the effect of pore-pressure in the overall material response. In this regard, and as discussed in the following sections, the experimental evidence demonstrates that the combined action of moisture and temperature diffusion may lead to accentuated concentrations of pore-pressure, causing great influence in the failure mode of concrete.

Thus, a simplified procedure is proposed to account for the pore vapor pressure evolution due to heating or cooling processes. This procedure allows to indirectly and effectively accounting for the

concrete hydraulic flux and drying processes during heating processes. Particularly, the following evolution law for the pore pressure is adopted

$$p_{vp} = \begin{cases} 0 & \text{if} \quad T \le 0 \\ p_{vp,0} e^{\alpha_{vp1}\left(T - T_{vp}\right)} & \text{if} \quad 0 < T \le T_{vp} \\ p_{vp,0} e^{-\alpha_{vp2}\left(T - T_{vp}\right)} & \text{if} \quad T > T_{vp} \end{cases} \tag{4}$$

where $p_{vp,0}$, T_{vp}, α_{vp1} and α_{vp2} are model parameters to be calibrated. Figure 4 illustrates the proposed p_{vp}-temperature rule, and its comparison against the experimental pore-pressure measurements by Pereira et al. [29] in concrete specimens subjected to heating.

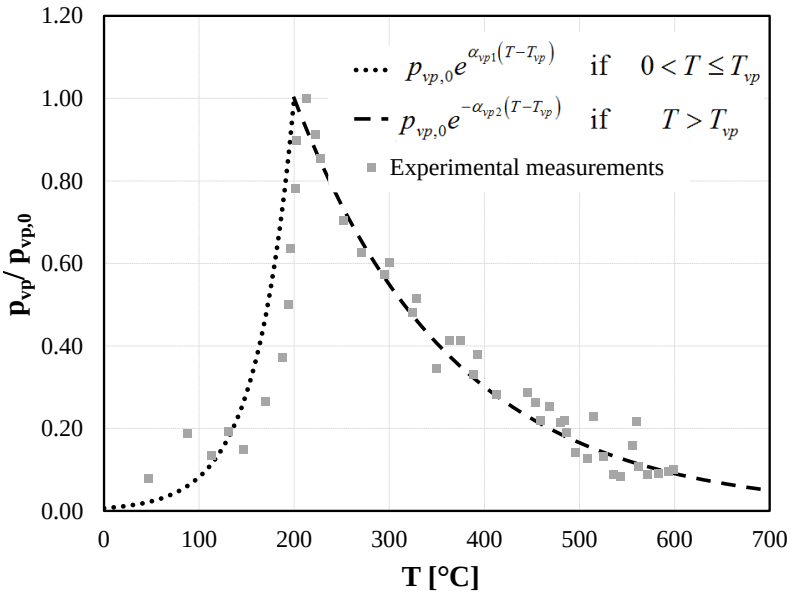

Figure 4: p_{vp} – temperature rule: comparison of the proposed law against poro-pressure experimental measurements on heated concrete speciments by Pereira et al. [29]: T_{vp}=200 °C, a_{vp1}= 0.025 and a_{vp1}= 0.006.

It is worth to mention that the proposed interface model allows to account for the pore-pressure concentration, caused by temperature diffusion, without involving complex hydro-thermomechanical coupling under temperature and moisture diffusion. This is clearly a simplified but highly effective procedure for analyzing such a complex phenomenon. Nevertheless, the current

241 formulation allows for a straightforward extension to also account for the moisture diffusion during
242 thermomechanical actions. This is currently under development by the authors in the framework of
243 multiscale homogenization procedures.
244

245 **3.3. Heat transfer across interfaces**

246 Heat transfer throughout an opened interface is governed by means of the following convective
247 interface rule [30]

$$q_n = -h_c \left[\left| \Delta T \right| \right] \tag{5}$$

248 which assumes a discontinuity in the temperature field

$$\left[\left| \Delta T \right| \right] = \left[\left| T^+ - T^- \right| \right] \neq 0 \tag{6}$$

249 being $\left[\left| \Delta T \right| \right]$ the norm of the temperature jump (across the interface), with T^+ and T^- the
250 temperatures on the + and - sides of the considered interface; h_c is the convective heat transfer
251 coefficient. Its value mainly depends on the normal relative displacement across the interface (u^+)
252 of the interface
253

$$h_c = h_c\left(u^+\right), \qquad h_0 \geq h_c \geq h_{\text{inf}} . \tag{7}$$

254 Particularly, h_c varies between a maximum value, h_0 related to the thermal conductivity, and a
255 minimum one h_{inf} which denotes the convective heat transfer coefficient for an open crack [21].

4. NUMERICAL EXAMPLES

In this section, the predictions of the proposed interface model for coupled thermo-mechanical failure analysis are evaluated under different temperature and mechanical conditions. Plenty of numerical analyses performed at constitutive, macroscopic and mesoscopic levels are presented and discussed regarding the combined temperature and pore-pressure effects on the developed failure mechanisms.

4.1. Residual strength test I: Calibration analyses at interface level

Direct tensile tests were performed for calibration purpose. Concrete specimens exposed to room, medium and high temperatures (at residual stages) are considered as reference. The numerical setup involves the calibration of a single contact (interface) as schematically presented in Figure 5.

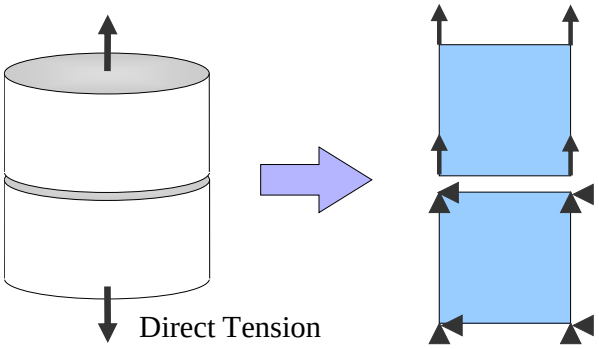

Figure 5: Setup of tensile tests.

Particularly, experimental results by Bamonte and Felicetti [33] were taken into account as benchmark for the numerical calibration. As a result of the calibration process, the temperature dependent decay function of the tensile peak strength highlighted in Figure 6 is updated. In this figure, the good agreement between this decay function and the experimental tensile peak strengths by Bamonte and Felicetti [33] can be observed. The resulting model parameters are reported in *Table 1*.

Table 1: Model parameters calibrated against the experimental results by Bamonte and Felicetti [33].

	Fracture/temperature-based model parameters [21]
Interface stiffness	$k_N = 500 MPa / mm$ $k_T = 200 MPa / mm$
Yield criterion	$\chi_0 = 4.0 MPa \quad c_0 = 7.0 MPa \quad \tan\phi_0 = 0.6$
Flow and softening rules	$\tan\beta = 0.3 \quad r_{tan\phi} = 0.67 \quad \sigma_{dil} = 10 MPa \quad \alpha_\chi = 0.5$
Fracture energies	$\sigma_{dil} = 10 MPa \quad \alpha_\chi = 0.5$
Temperature-based rule	$T_{avg,0} = 20^o C \quad T_{avg,f} = 1500^o C \quad \varsigma_\chi = \varsigma_{d_\tau} = -1.8$

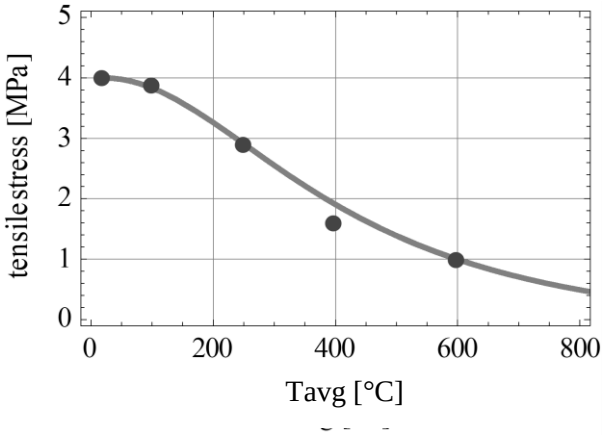

Figure 6: Strength decay in direct tensile tests: experimental results (dots) [33] vs. model predictions (continuous curve).

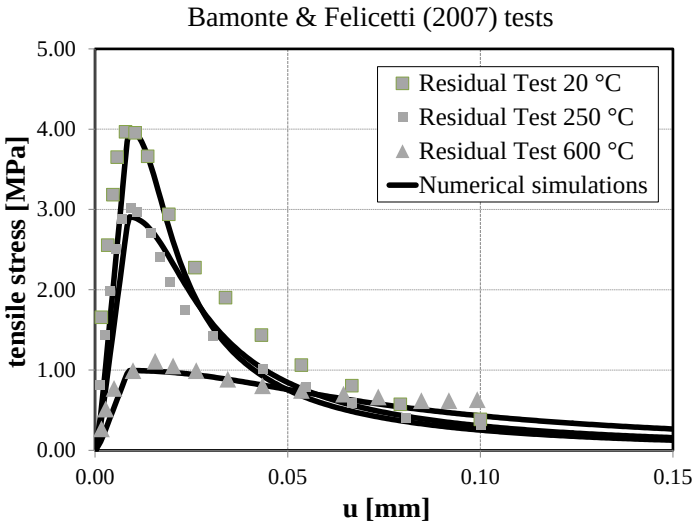

Figure 7: Tensile stress vs. crack opening curves: experimental (residual) results [33] against numerical predictions.

Figure 7 shows the comparisons between the experimental and numerical results in terms of tensile stress vs. crack-opening displacements for the three different temperature levels. It figures out accurate predictions of the interface model not only regarding stiffness and peak strength, but also concerning the temperature dependent post peak behavior. Beyond the soundness and capability of the interface proposal in predicting failure behavior of concrete affected by temperature, the numerical results demonstrate the capabilities of the discontinuous formulation to reproduce the strong thermal sensitivity of concrete mechanical behavior in its whole range.

The complete description of these numerical tests, the adopted calibration and their validation against experimental data were proposed and extensively discussed in a previous work published by the authors; see Caggiano and Etse [21]. The exhaustive discussion is here omitted for the sake of brevity.

4.2. Residual strength tests II: Predictive analyses at macroscopic level

In the next series of analyses a simple shear test, schematically shown in Figure 8, is proposed on concrete frames subjected to room, medium and high temperature. The same material parameters of Section 4.1 have been employed with this purpose.

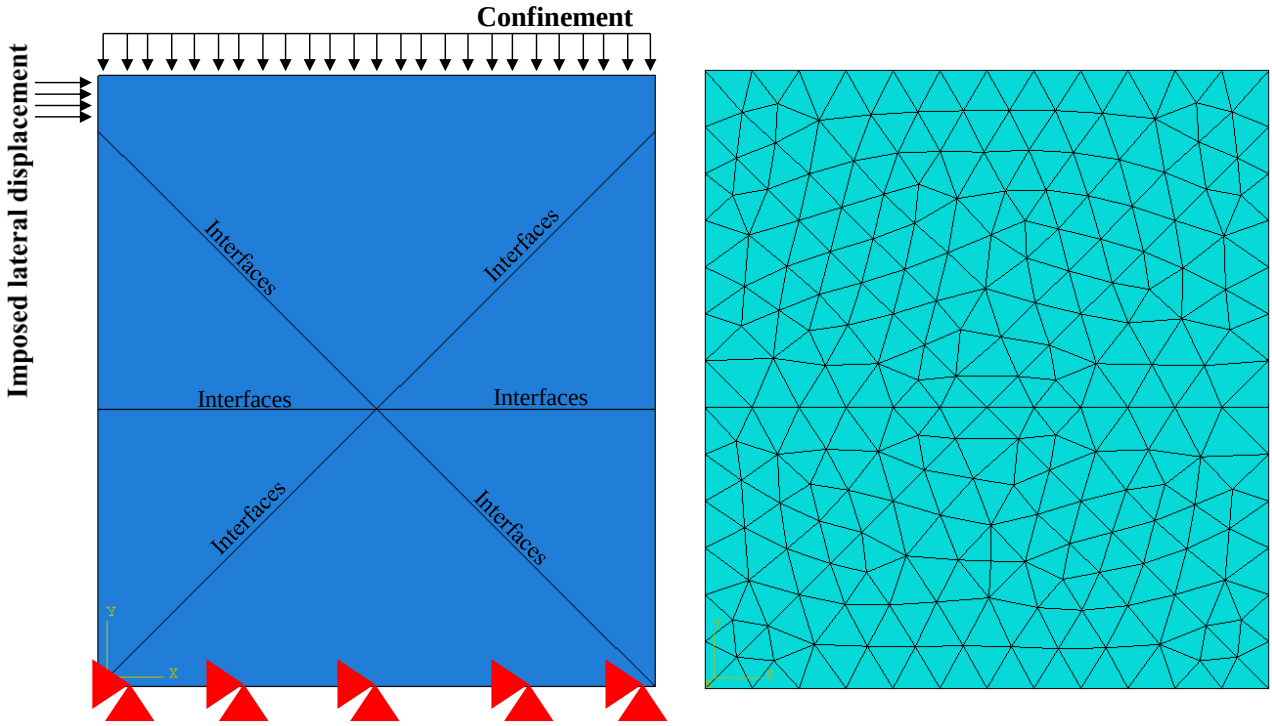

Figure 8: Geometry and boundary condition of a direct shear wall (100×100×10 cm^3).

Main goal of these analyses is to evaluate the capability of the proposed interface formulation within a macroscopic FE discretization to predict the structural response and its mechanical degradation due to temperature in direct shear. For this purpose, the FE arrangement exhibited in Figure 8 of the concrete wall in residual condition, and subjected to vertical pressure and lateral shear, is considered. Altogether, 708 nodes and 2141 4-node bi-linear and poroelastic finite elements, under plane stress conditions, were considered in this domain discretization. The nonlinear poroplastic interfaces were included along the contact lines between continuum finite elements indicated on the right hand side of Figure 8. Geometrical dimensions of the concrete wall are 100×100×10 cm^3. Different confinement pressures were applied on the top surface and the lateral shear was applied under displacement control.

Figure 9 shows the numerical predictions in terms of the shear load versus lateral displacement at room temperature. As expected, it can be observed a strong influence of the applied vertical pressures in the initialization of the cracking mechanism, exhibiting higher cracking resistance and

less failure location as the vertical pressure increases. As a result, a steeper post-peak response is observed in those specimens under low (or zero) confinement.

Figure 10 shows the results corresponding to specimens subjected to pure shear (no confinement). These analyses focus on the temperature effects in concrete walls failure behavior under simple shear. As it can be observed, the cracking or macroscopic damage in the pre-peak regime reduces with temperature. However, due to degradation of the concrete/mortar mechanical features, the overall stiffness decreases, while the axial displacement at peak load increases with temperature. The results under medium and high temperatures also illustrate the significant influence of the thermal effects on the post-peak ductility. Altogether these results demonstrate that high temperature induces relevant changes and degradations on the fundamental structural features of concrete components subjected to simple shear which result in dramatic modifications of the strength capabilities and involved kinematics. The latter may lead to severe and sudden structural instabilities.

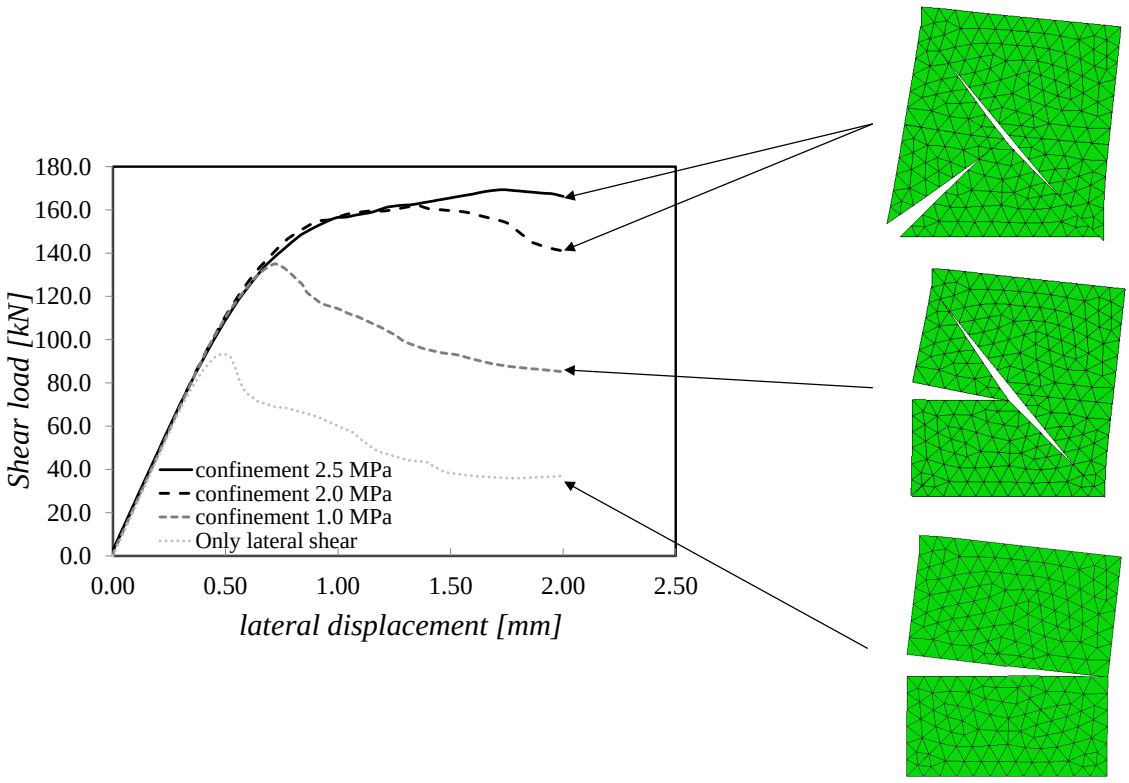

Figure 9: Shear load-displacement responses and failure crack configurations: test results at T=20 °C and different vertical confinement levels.

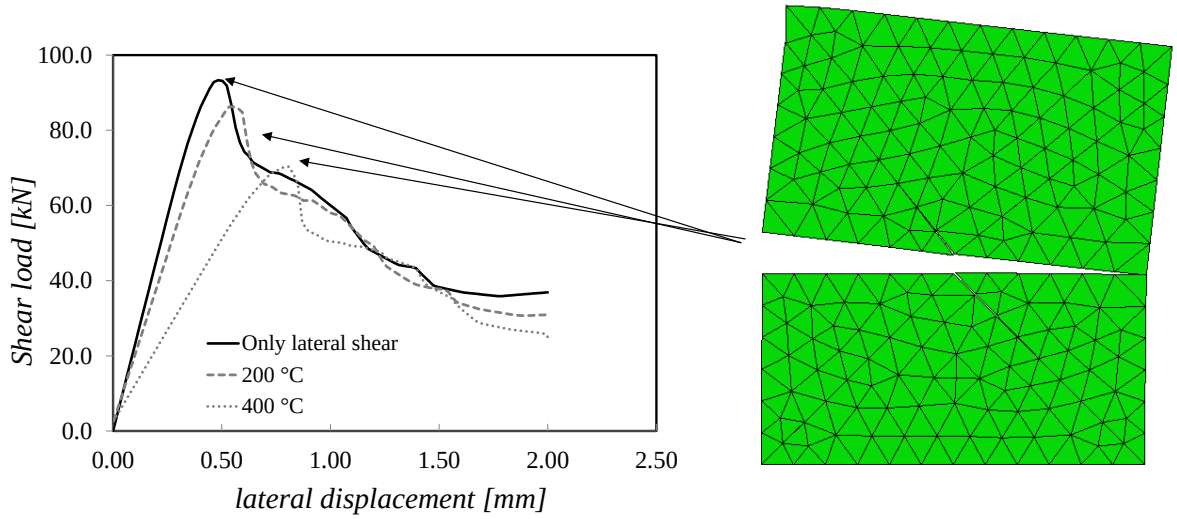

Figure 10: Shear load-displacement responses and failure crack configurations: vertical confinement level considered null and variable temperatures.

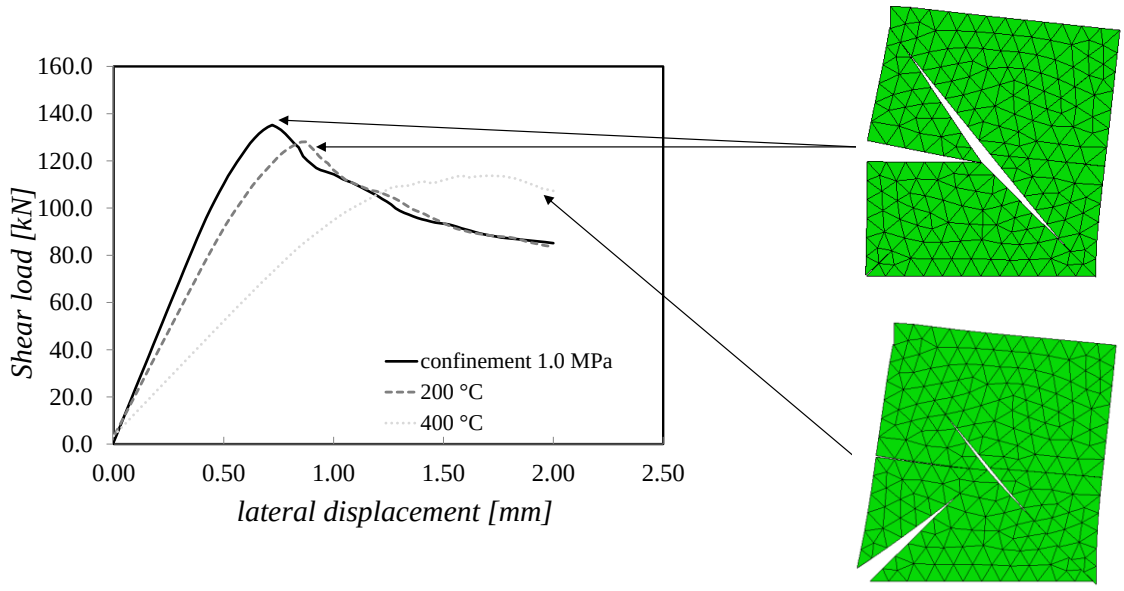

Figure 11: Shear load-displacement responses and failure crack configurations: vertical confinement level of 1.0 MPa and variable temperatures.

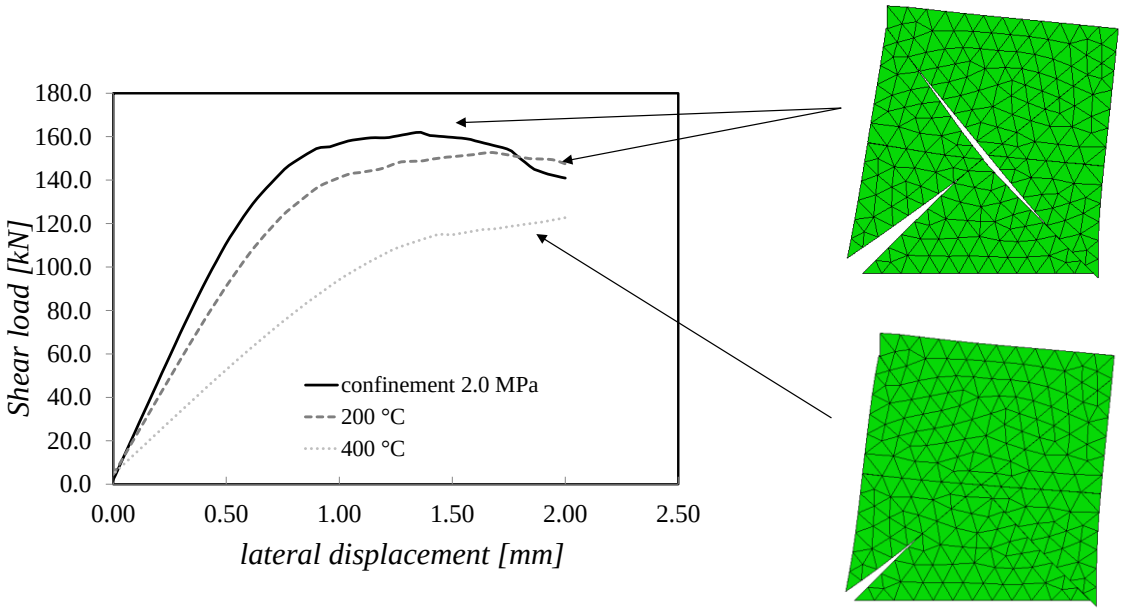

340

341 *Figure 12: Shear load-displacement responses and failure crack configurations: vertical*

342 *confinement level of 2.0 MPa and variable temperatures.*

343

344 Figure 11-13 present the numerical results corresponding to the shear panels when the combined

345 effects of vertical pressure and temperature were applied. Particularly, in Figure 11, for the low

346 confinement level (1.0 MPa) a similar failure behavior to the non-pressure case can be observed in

347 terms of shear load versus lateral displacement. This means that the larger the temperature the lower

348 the peak-stress and the larger the peak-load displacements. Similar post-peak responses can be

349 observed for room temperature and 200 °C.

350 Figure 12 shows the results under medium confinement (i.e., 2.0 MPa). Thereby, an increasing post-

351 peak ductility can be observed for all temperature cases, which is manifested in a much less steeper

352 softening curve. Same trend but with an even softer response can be observed for the highest

353 applied pressure (2.5 MPa) in Figure 13.

354

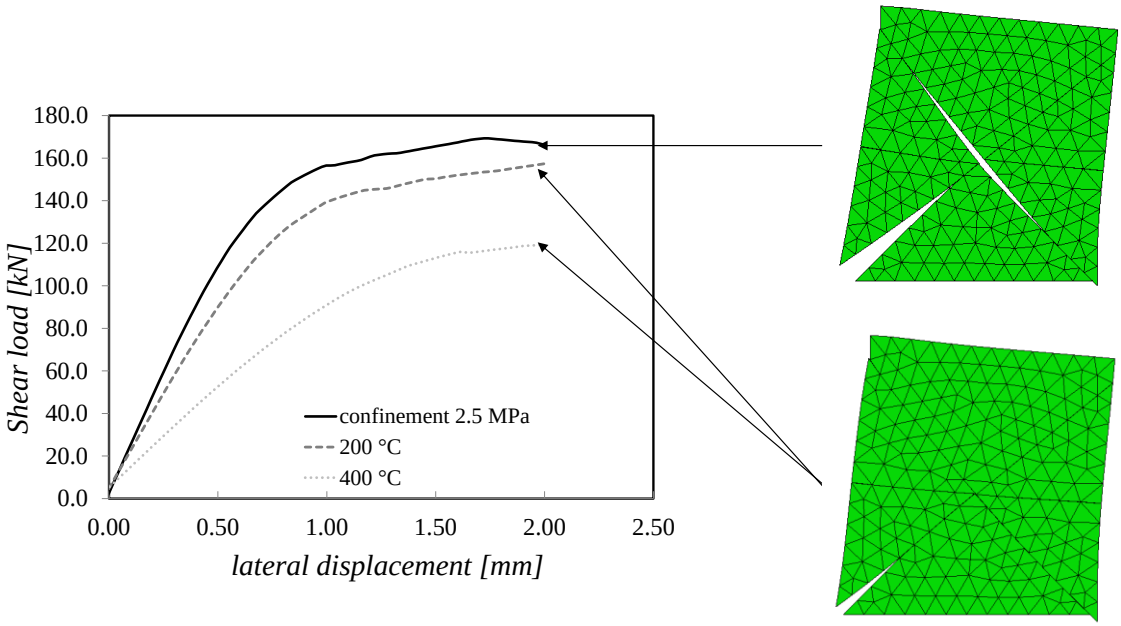

Figure 13: Shear load-displacement responses and failure crack configurations: vertical confinement level of 2.5 MPa and variable temperatures.

4.3. Concrete panel subjected to fire

In this section, a numerical transient analysis is performed on a 12-cm thick concrete panel when subjected to fire exposure on one side (Figure 14). Considered fire action follows the standard ISO-834 fire for buildings as indicated in Figure 15. The FE discretization involves 1780 nodes and 89 plane strain eight-node coupled temperature-displacement elements.

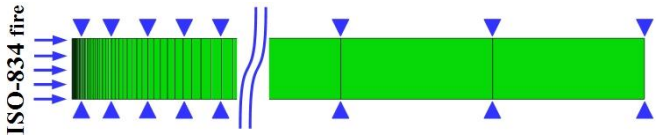

Figure 14: Schematic representation of the geometry and boundary conditions of analysis.

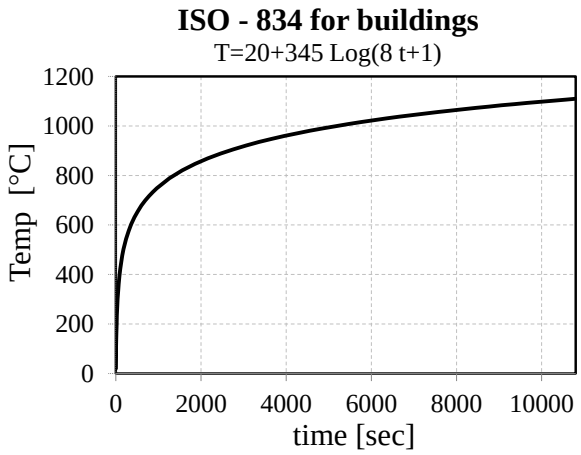

Figure 15: Temperature development ("fire curve") for buildings namely ISO-834.

As can be observed in Figure 16 the heating gradually propagates from the panel surface subjected to fire (under Dirichlet boundary conditions) to the panel center through the solid poroelastic FEs. Consequently, and due to the temperature dependent pore-pressure law of the proposed interface model, this fundamental variable of the concrete porous phase evolves in time and panel-width spaces as indicated in Figure 17. As it can be seen from Figure 16 and 17, the maximum vapor poro-pressure (0.7-0.8 MPa) takes place in the region of the concrete panel width where the temperature reaches values approximately equal to 200 °C.

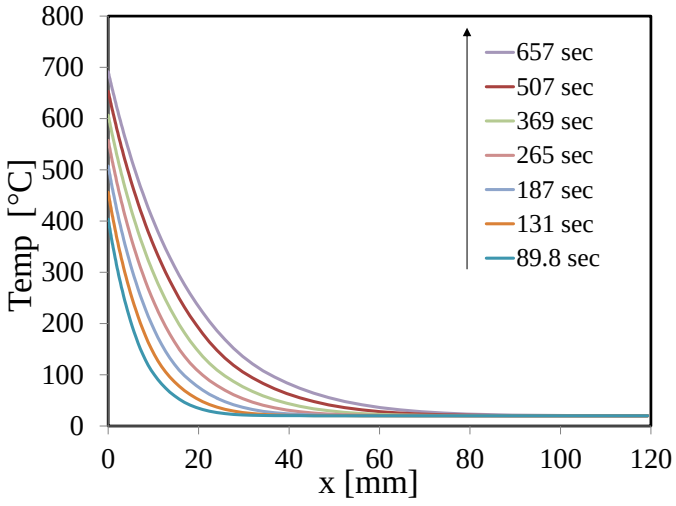

Figure 16: Temperature across the wall (X coordinate) for different times of analysis.

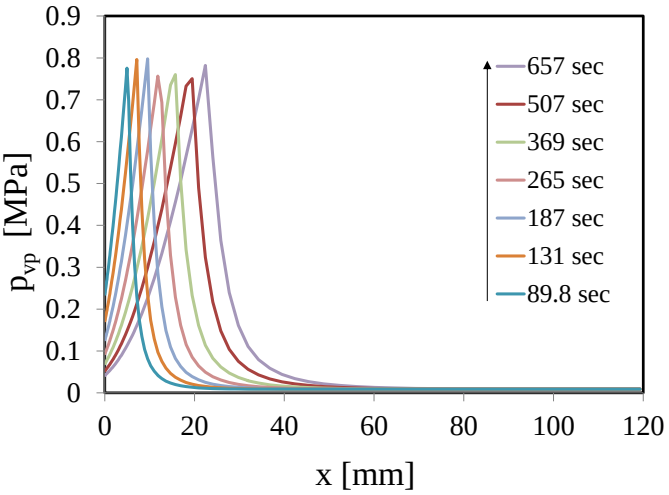

Figure 17: Pore-pressure across the wall (X coordinate) for different times of analysis.

The predictions of temperature and pore-pressure evolutions in heated concrete panels obtained with the proposed poroplastic interface model in this work, agree very well with other numerical results which are available in the scientific literature related to high temperature tests on concrete components, see [35][36][37][38].

4.4. Coupled thermo-mechanical test in tensile mode

In this section, coupled thermo-mechanical tests on concrete specimens under tensile mode, as shown in Figure 5, are numerically performed to evaluate the overall interface model performance under more general multiphysical actions. The concrete specimen discretization and thermomechanical boundary conditions are shown in Figure 18. Assumed thermal parameters for the thermo-mechanical coupling are listed in

Table *2*.

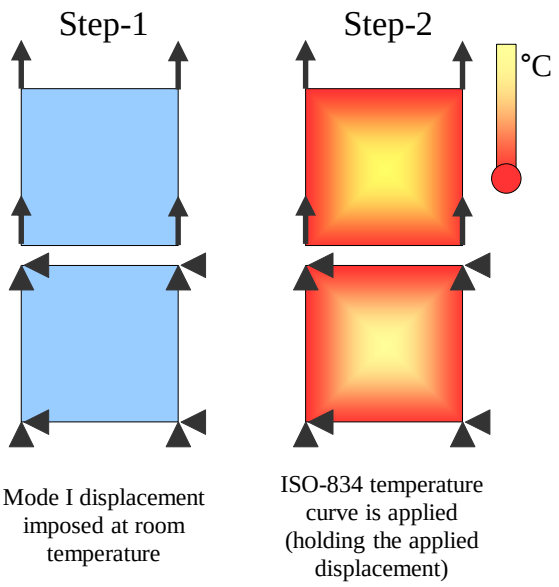

Figure 18: Specimen geometry, boundary conditions and considered steps.

Two numerical analyses were performed, one including the temperature-dependent pore-pressure law detailed in Section 4.3, while in the second one the pore-pressure was assumed as temperature independent.

Figure 19(a) illustrates the applied interface normal separation vs. temperature variation during the numerical tests. Firstly pure mode I fracture displacements were imposed under room temperature (i.e., 20 °C); then the ISO-834 temperature curve was applied to the whole specimen, while keeping fixed the tensile displacement (similarly to the well-known relaxation test but under heating), see Figure 18. Figure 19 (b) and (c) show the obtained results in terms of stress vs. interface separation and stress vs. temperature, respectively.

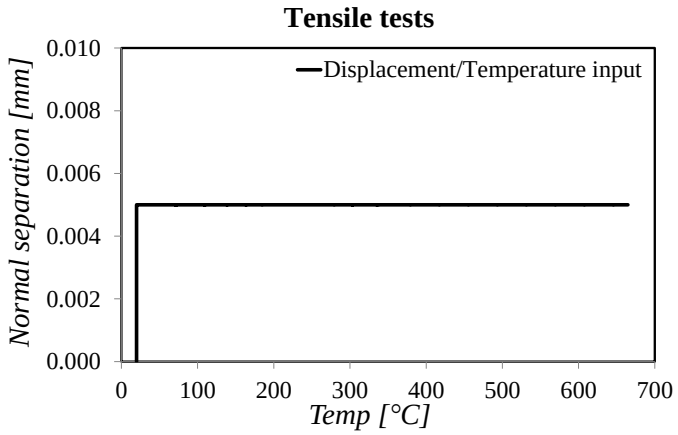

(a)

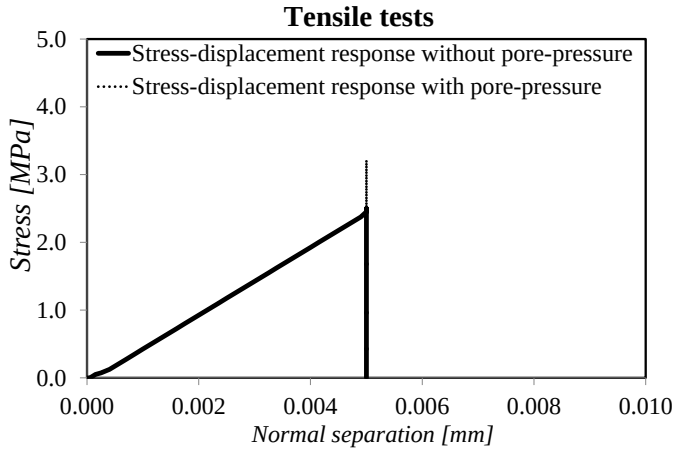

(b)

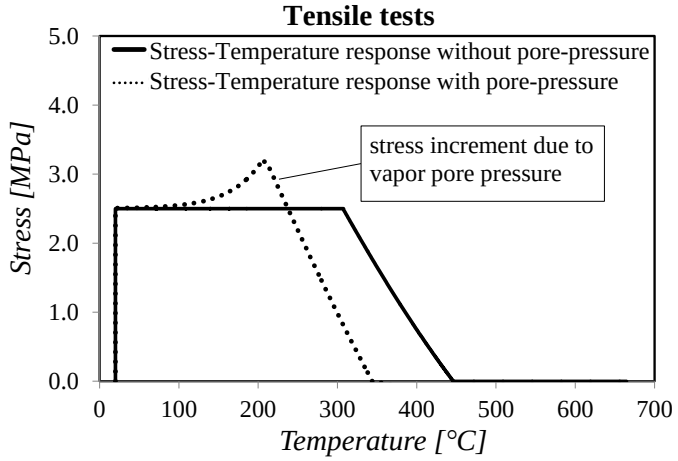

(c)

Figure 19: (a) displacement-temperature input history, (b) normal stress vs. interface opening displacements and (c) stress-temperature response.

Table 2: Thermal parameters of concrete according to EN 1992-1-2:2004 [34].

T [°C]	c_p [J kg^{-1} °C^{-1}]	λ [W m^{-1} °C^{-1}]	ε_{th} [-]	T [°C]	ρ[kg m^{-3}]	E [GPa]	ν [-]
20	900	1.642	1.12E-07	20	2300	38.200	0.200
100	1470	1.498	4.94E-04	100	2300	33.922	0.184
200	1000	1.332	1.19E-03	200	2254	28.574	0.164
400	1100	1.049	3.18E-03	400	2185	17.878	0.124
500	1100	0.932	4.63E-03	500	2165	12.530	0.104
600	1100	0.832	6.50E-03	600	2145	7.182	0.084
700	1100	0.748	8.88E-03	700	2125	1.834	0.064
734	1100	0.723	9.82E-03	734	2118	0.015	0.057
800	1100	0.680	1.18E-02	800	2105	0.015	0.057
900	1100	0.629	1.20E-02	900	2084	0.015	0.057
1000	1100	0.595	1.20E-02	1000	2064	0.015	0.057
1100	1100	0.576	1.20E-02	1100	2044	0.015	0.057
1200	1100	0.574	1.20E-02	1200	2024	0.015	0.057

As expected, the temperature-dependent pore-pressure behavior leads to increments of the effective normal stress during heating and, therefore, the interface failure surface is approached at lower temperature (209 °C) than in the case of temperature-independent pore-pressure (310 °C). Consequently, the degradation process of the interface state parameters start earlier during the heating process and the complete failure of the specimen (reached when the tensile stress becomes zero) takes place at lower temperature (343 °C) in case of the temperature-dependent pore-pressure law, as compared to the temperature-independent case (446 °C).

4.5. Coupled thermo-mechanical analyses of concrete failure behavior at mesoscopic level

For the purpose of these numerical analyses, the mesoscopic FE discretization of 100×100 mm^2 concrete specimens shown in Figure 20 was adopted. This is based on a 6×6 arrangement of coarse aggregates embedded in a cementitious matrix. This mesoscopic geometry is characterized by an average aggregate size of 17.33 mm and a volume fraction of 0.45. The reference mesh, see

Figure 2, is composed by 8440 nodes, 5020 4-nodes isoparametric plane stress elements and 1814 contact interfaces. Continuum elements representing coarse aggregates and mortars were assumed as linear thermoelastics while non-linear, temperature-dependent, interfaces were lumped at all mortar-to-mortar and aggregate-to-matrix joints.

Table 3: Thermal-based parameters for the mesoscopic numerical analyses.

T [°C]	c_p[J kg^{-1}°C^{-1}]	λ [W m^{-1}°C^{-1}]	ρ [kg m^{-3}]	E [GPa]	ν [-]	α [°C^{-1}]
20	900	1.64	2300	3.82E+01	0.200	5.00E-06
99	900	1.50	2300	3.40E+01	0.184	5.00E-06
100	1470	1.50	2300	3.39E+01	0.184	5.00E-06
115	1470	1.47	2300	3.31E+01	0.181	5.00E-06
185	1083	1.36	2268	2.94E+01	0.167	5.00E-06
200	1000	1.33	2254	2.86E+01	0.164	4.49E-06
300	1050	1.18	2220	2.32E+01	0.144	2.38E-06
400	1100	1.05	2185	1.79E+01	0.124	1.80E-06
500	1100	0.93	2165	1.25E+01	0.104	1.59E-06
600	1100	0.83	2145	7.18E+00	0.084	1.57E-06
700	1100	0.75	2125	1.83E+00	0.064	1.56E-06
720	1100	0.73	2121	7.64E-01	0.060	1.55E-06
734	1100	0.72	2118	1.53E-02	0.057	1.55E-06
800	1100	0.68	2105	1.53E-02	0.057	1.54E-06
900	1100	0.63	2084	1.53E-02	0.057	1.52E-06
1000	1100	0.59	2064	1.53E-02	0.057	1.50E-06
1100	1100	0.58	2044	1.53E-02	0.057	1.50E-06
1200	1100	0.57	2024	1.53E-02	0.057	1.50E-06

In the mesoscopic numerical analyses, interface elastic stiffness in both normal and tangential directions (k_N and k_T, respectively) were set as high as possible and compatible with numerical conditioning [39] in order to obtain thermo-elastic responses which are mainly controlled by the temperature-based deformation of the continuum elements. Elastic material parameters at 20 °C were assumed as: aggregates $E = 70.0$ *GPa*, mortar matrix $E = 38.2$ *GPa* and $\nu = 0.2$ (Poisson ratio) for both of them. Considered temperature-dependent parameters and thermal variables for

the aggregates were: $\lambda = 0.04\ W\times m^{-1}\times °C^{-1}$, $c_p = 790\ J\times kg^{-1}\times °C^{-1}$, $\alpha = 1.25\times 10^{-6}\ °C^{-1}$ and $\rho = 2300\ kg\times m^{-3}$; while that for the mortar are listed in Table 3. For mortar-mortar interface: $k_N = 500$ MPa/mm, $k_T = 200$ MPa/mm, $tan\phi_0 = 0.6$, $tan\beta = 0.3$, $r_{tan\phi} = 0.67$, $\chi_0 = 3.0$ MPa, $c_0 = 6.5$ MPa, $G_f^I = 0.07$ N/mm, $G_f^{IIa} = 0.7$ N/mm. For all other parameters, the same values to those informed in Caggiano and Etse [21] were assumed. Mortar-aggregate parameters agree with those of the mortar-mortar interfaces with exception of $\chi_0 = 2.0$ MPa, $c_0 = 4.5$ MPa, $G_f^I = 0.05$ N/mm and $G_f^{IIa} = 0.5$ N/mm. Finally, considered thermal and dehydration parameters were those indicated in Section 4.1 and 4.4.

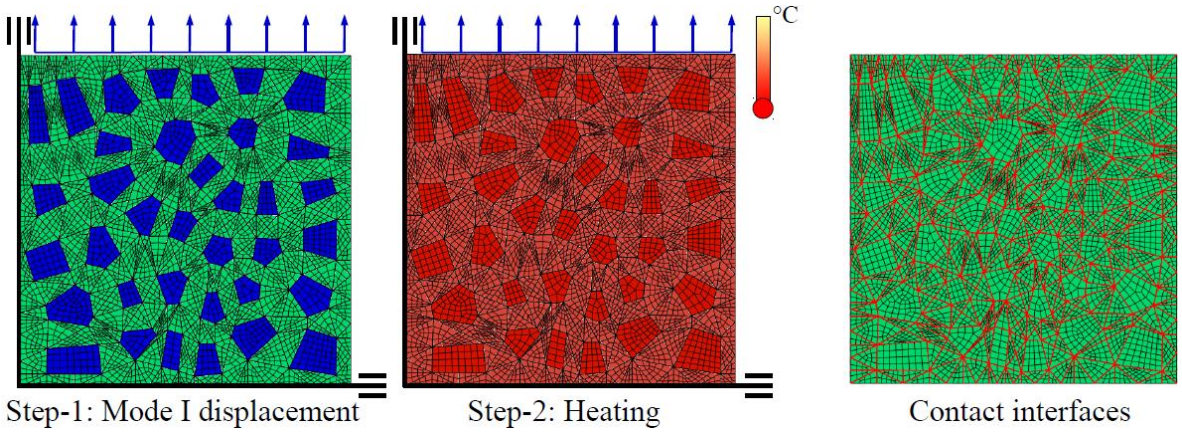

Figure 20: Coupled thermo-mechanical meso-scale analysis with two-step simulations: mesh, boundary conditions and interfaces.

4.5.1. Mesoscopic thermo-mechanical tensile tests

Numerical analyses at mesoscopic level under tensile loading combined with heating are described in this section. As shown in Figure 20 the mesoscopic analyses involved two phases: a first phase (or step-1) under pure uniaxial tensile displacements at room temperature, and a second phase (or step-2), where the ISO-FIRE 834 heating (Figure 15) was applied, while keeping constant the lately reached vertical displacement in step-1. Particularly, in step-1 vertical displacement increments were uniformly applied in all nodes of the upper mesh side. Symmetry boundary

conditions were applied on the left and bottom sides of the specimen. In the second phase two different heating cases were alternatively evaluated: (i) heating is applied in all mesh nodes and (ii) heating is only applied along the specimen contour (i.e. all nodes along the right and upper sides, where Dirichlet boundary conditions were considered). Case (i) represents the heating process in a relatively narrow concrete panel where the fire action involves the entire panel volume while case (ii) represents the heating process in a column or long concrete element, where fire action only affects the element perimeter.

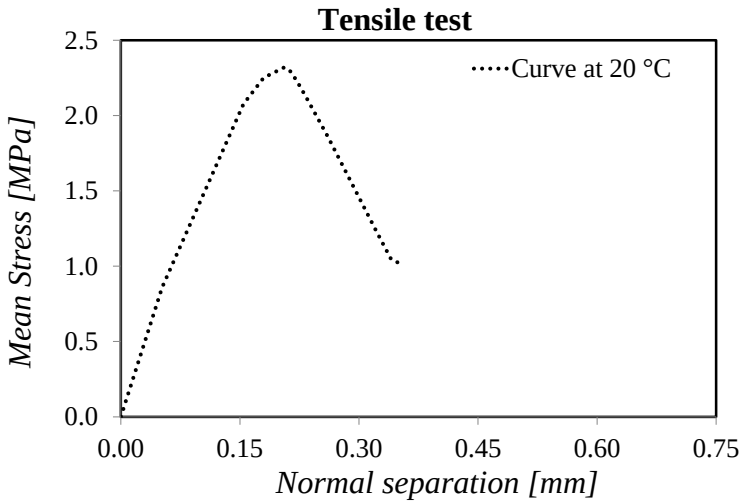

(a)

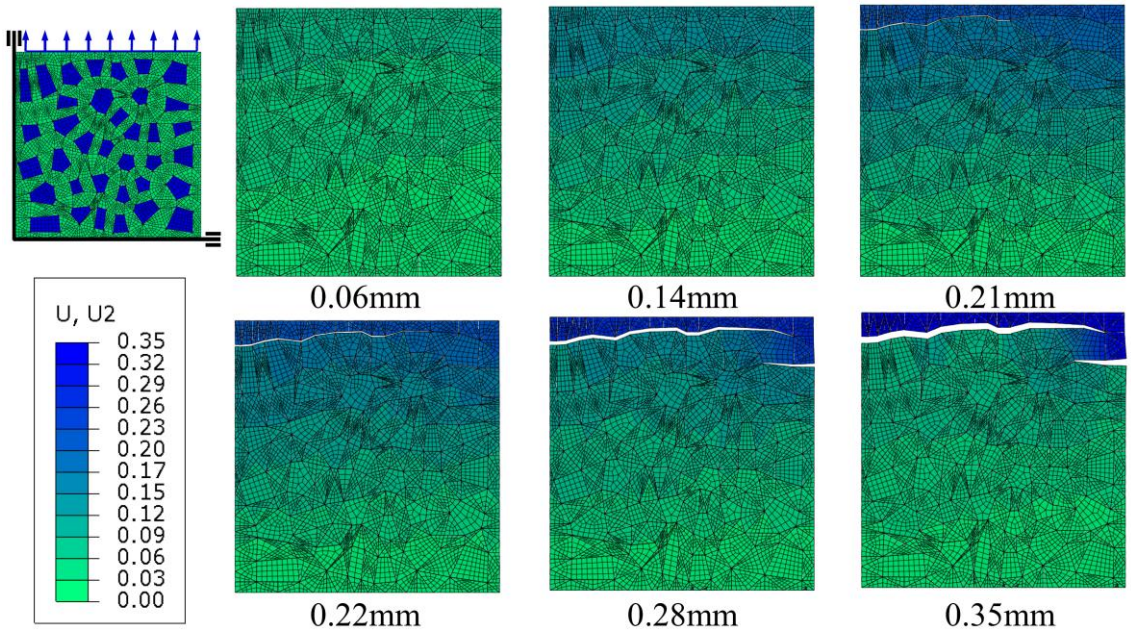

(b)

Figure 21: Imposed tensile displacements (STEP-1: 20 °C): (a) stress-normal separation response and (b) crack configurations (deformation scale factor ×10).

The results obtained during step-1, under 20°C, are plotted in Figure 21. The curve representing the obtained response behavior in terms of the average stress (obtained by dividing the sum of all nodal vertical reactions times the specimen length) versus the applied vertical

489 displacement is highlighted in Figure 21(a). The cracking evolution at the mesoscopic level of
490 observation during step-1 can be observed in Figure 21(b).

491 Four different analyses were performed to simulate concrete behavior during the step-2 or
492 heating phase, as follow:

493 • **all+Hy+Pp**: Heating case (i) was applied (all nodes affected), while interfaces with
494 dehydration functions (temperature-dependent interface model [21]) and temperature-
495 dependent pore-pressure rule were assumed;

496 • **all+Hy-Pp**: Heating case (i) and interfaces with dehydration functions and temperature-
497 independent pore-pressure;

498 • **UR+Hy+Pp**: Heating case (ii) and interfaces with both dehydration functions and
499 temperature-dependent pore-pressure;

500 • **UR+Hy-Pp**: Heating case (ii) and interfaces with dehydration functions and temperature-
501 independent pore-pressure.

502 Temperature-dependent results of the aforementioned 4 analyses can be observed in Figure
503 22. Altogether, six different levels of maximum pre-imposed vertical displacement were reached in
504 step-1: 0.10, 0.15, 0.20, 0.25, 0.30 and 0.35 mm. From each one of these reached pre-cracking
505 vertical displacements under room temperature, the heating process started during step-2, and the
506 corresponding evolution of the mean stress in term of the applied temperature is shown in each one
507 of the 6 diagrams in Figure 22. As it can be observed, the temperature dependency of the pore-
508 pressure strongly influenced the overall response, see curves +Pp vs. –Pp, and so it does the type of
509 heating affecting the concrete element, i.e. case (i) (curves all) or (ii) (curves UR).
510

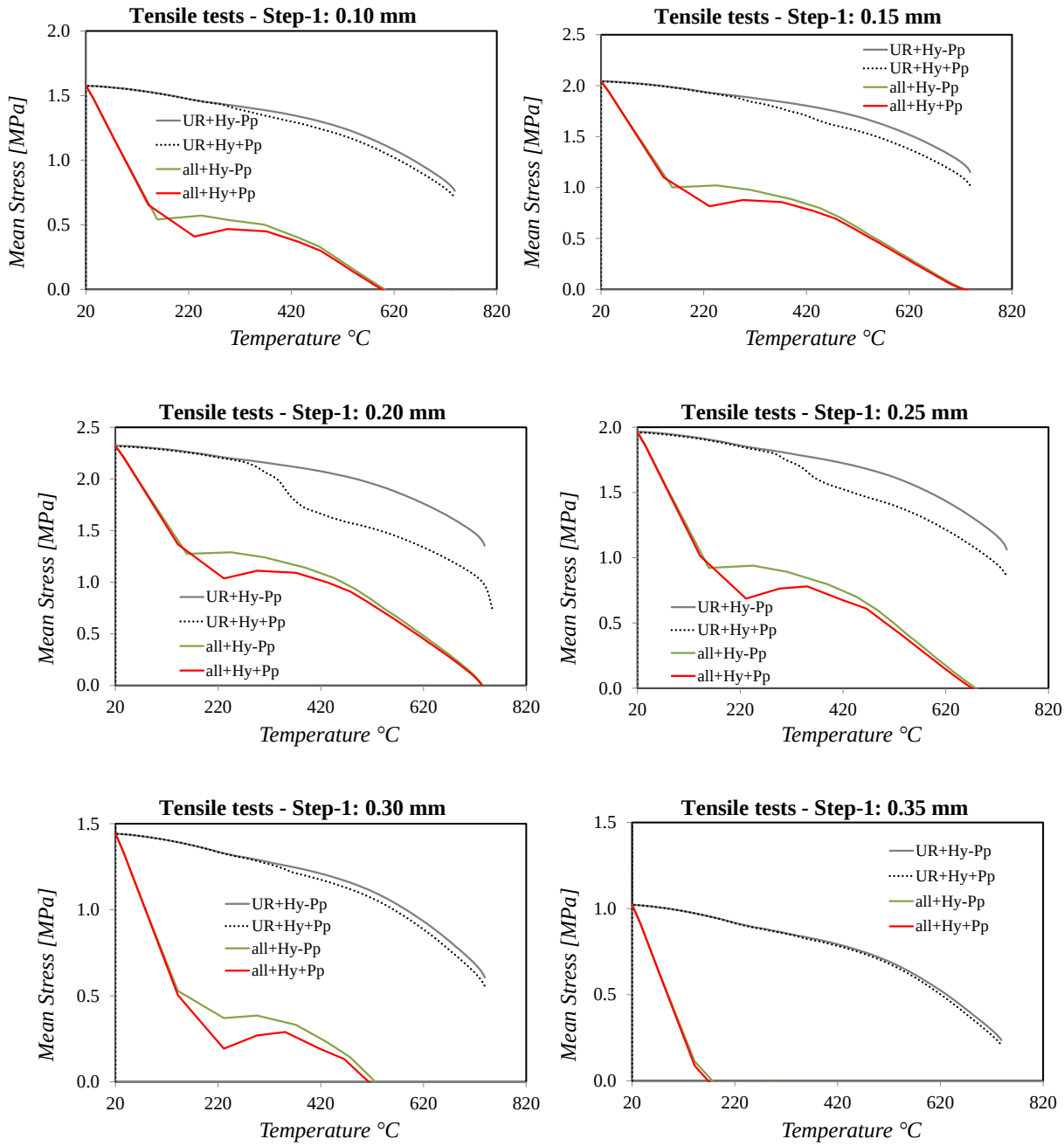

Figure 22: Tensile stress-temperature response for six pre-stretched levels (step-1) and four boundary step-2 conditions.

The numerical results highlight that the stress relaxation rate under heating in step-2 is higher when the complete mesh is affected by the increasing temperature. At low and middle initial (or pre-stretched) vertical displacements (e.g., up to 0.30 mm), the temperature dependency of the pore-pressure affects more significantly the stress relaxation processes of the tests under heating case (i)

(all nodes affected). However, when middle initial pre-imposed vertical displacement was reached in step-1 (e.g., 0.15, 0.20 and 0.25 mm), the temperature dependency of the pore-pressure affects more those relaxation curves corresponding to heating case (ii) (heating nodes along the right and upper sides). It can also be observed that the stress relaxation processes of the tests under heating case (i), where all mesh is heated, is characterized by an apparent recovery (namely, stress-temperature "re-hardening") of the mean stress (see between 200 and 350 °C of the tests "all" in Figure 22). This phenomenon, occurring for 5 of the 6 analyzed "all" cases (Figure 22), can be explained as result of the thermal expansions occurred in the continuous elements during temperature rises which try to close the active cracks and for that producing an increment of the overall post-cracking strength of the analyzed meso-specimens. Then, for temperatures beyond the 350/400 °C the effect of the de-hydration rule affecting the internal parameters of the cracking criteria allowed to reach the complete failure of the specimens. This effect did not occurred for the tensile tests in which the step-1 was followed up to 0.35 mm (maximum pre-imposed displacement) being in this case the opened cracks sufficiently high to be not influenced by the thermal expansion of the material. Moreover, all tests of Figure 22 with the case (ii) "UR" of heating did not register, as expected, such a stress recovery response: i.e., the temperature rises throughout these meso-specimens were much lower than those cases in which the whole panel was heated. Hence, a lower thermal expansion (aimed at acting as crack-closing) interested the UR tests. Figure 23 reports the crack evolution during the heating cases (i) and (ii) on the specimen previously subjected to pre-stretched displacement (step-1) of 0.35 mm.

The results in Figures 21 to 23 demonstrate the soundness of the interface model and numerical tools to analyze the failure behavior of concrete components under coupled thermo-mechanical actions. They also demonstrate that the temperature dependent pore-pressure assumption in this interface model provides an effective and quite simple methodology to indirectly account for the drying effects and changes in the concrete hydraulic flux due to temperature.

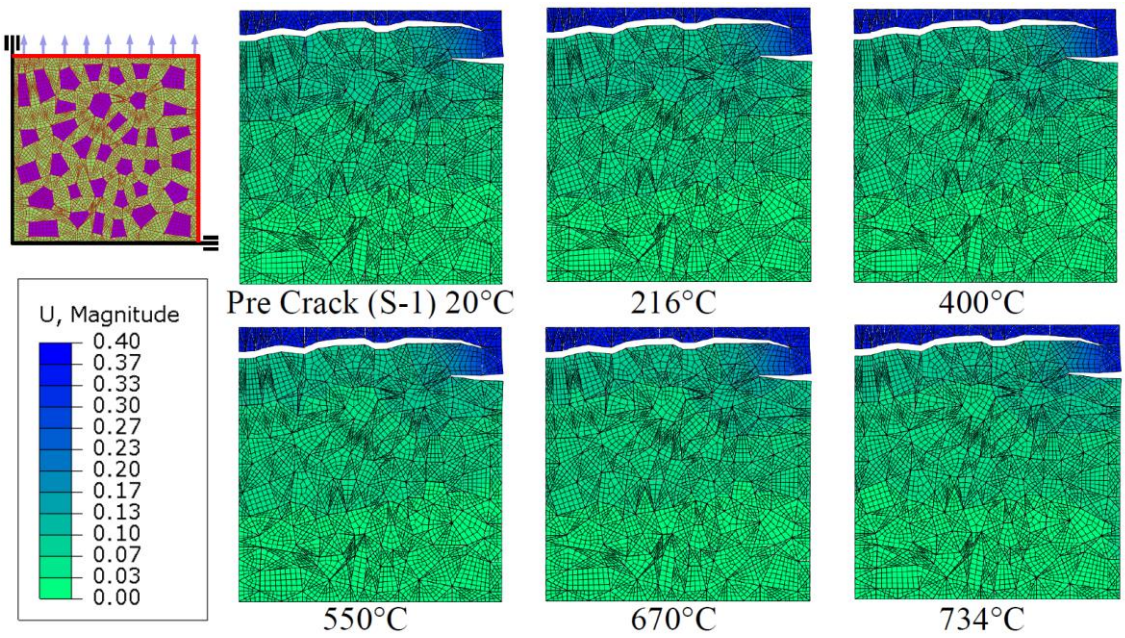

(a)

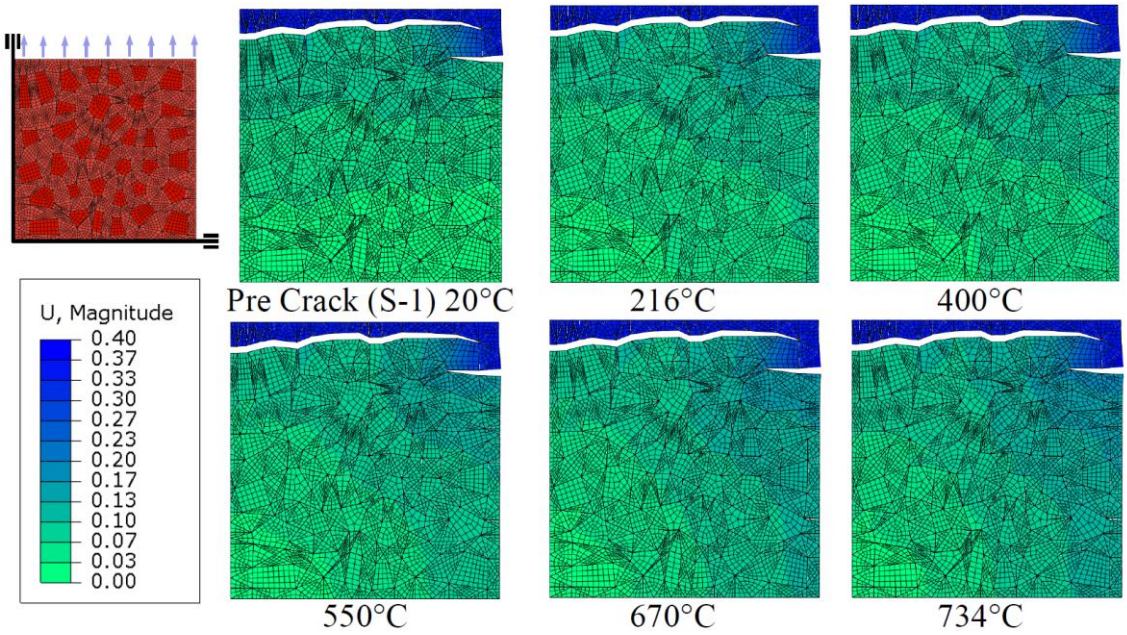

(b)

Figure 23: Crack configurations with a pre-stretched level (step-1) of 0.35 mm: (a) UR+Hy+Pp and (b) all+Hy+Pp (deformation scale factor ×10).

555 **4.5.2. Mesoscopic thermo-mechanical compression tests**

556 Meso-scale tests under compression combined with heating are described in this section in a
557 similar way of the previous tensile analyses. Thus, the concrete specimen at mesoscale level of
558 Figure 20, with similar boundary conditions, was subjected to 2 sequential loading steps. Firstly,
559 uniaxial compression in vertical direction under displacement control and room temperature was
560 applied. In the second phase (or step-2), the ISO-FIRE 834 heating (Figure 15) was enforced,
561 keeping constant the pre-imposed compression displacements reached in step-1. As for the tensile
562 cases, two different heating cases were considered: (i) heating in all mesh nodes and, (ii) heating
563 along the specimen's contour.

564 The results obtained during step-1 (at 20 °C) are shown in Figure 24. As before, average
565 compressive stresses are obtained by dividing total vertical reaction by the specimen's cross-
566 section. Figure 24(a) shows the mean stress vs. vertical displacement curve while the crack
567 evolutions and configurations at several loading stages during step-1 are represented in Figure
568 24(b).

569 The same four analyses (*all+Hy+Pp, all+Hy-Pp, UR+Hy+Pp* and *UR+Hy-Pp*) proposed for
570 the tensile cases, as described in the previous section, were considered during the step-2 (heating
571 phase). Temperature-dependent results of these 4 cases can be observed in Figure 25. For the
572 compression cases four pre-compressive levels were considered in step-1: -0.50, -0.75, -1.00 and -
573 1.125 mm, respectively. From each one of these reached pre-vertical displacements at 20 °C, the
574 heating process started during step-2, and the corresponding evolution of the mean compressive
575 stress in term of the applied temperature is shown in each one of the 4 graphs of Figure 25. It can be
576 observed that the responses are mainly influenced by the increasing temperature field and are quite
577 insensible to the pore-pressure effects (see curves +Pp vs. -Pp). These quite different results to those
578 obtained in the tensile tests can be better understood by analyzing the micro- and macro-crack
579 evolutions in the compressive tests (Figure 26). Damage and strain localizations under compression

are clearly characterized by inclined shear bands and mode II of fractures. In these fracture modes, and related stress states, the pore-pressure has very limited (or directly non) effect. Only in tensile failure forms, under fracture mode I, the normal interface stresses, which control the failure process, are highly sensitive to the pore-pressure. This is the reason why only the tensile tests (and not the compression ones) are considerably influenced by Pp.

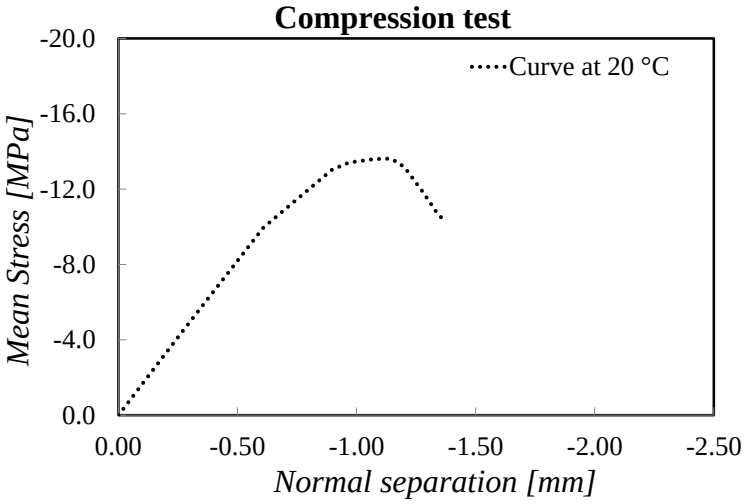

(a)

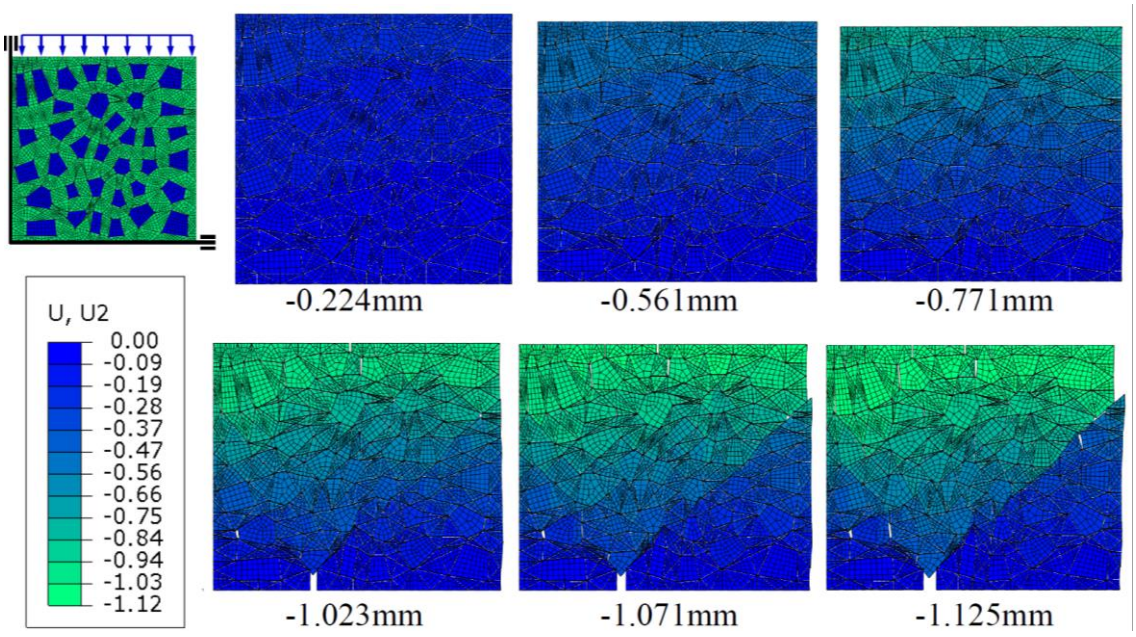

(b)

Figure 24: Imposed compression displacements (STEP-1: 20 °C): (a) stress-normal separation response and (b) crack configurations (deformation scale factor ×10).

The numerical results demonstrate that the stress relaxation rate during heating is more significant when the whole concrete specimen is affected by the temperature rise. It can be observed that when low and middle pre-compression levels were reached in phase 1 (vertical displacements of -0.50 and -0.75 mm), for the heating case (i) (entire specimen subjected to heating) a re-hardening effect takes place during first part of phase II. This effect, occurring in 2 of the 4 analyzed cases of Figure 25, deals with the concrete thermal expansions which in this numerical tool is capture by the thermoelastic formulation of the continuous elements. Actually, this thermal expansion gives rise to an additional "confinement" and, therefore, to an increase of the overall concrete cracking strength. Continuing with these cases and when middle and, moreover, high temperatures are reached during phase 2, and due to de-hydration rule affecting the internal parameters of the interface yielding/cracking criteria, the complete failure of the concrete specimen is obtained. The thermal expansion phenomenon during heating strongly reduces in those concrete specimens where the compressive stress reached in phase 1 is high (maximum vertical displacements at the end of step 1 of -1.00 mm and -1.125 mm). This is because the strong concrete mechanical damage reached during the purely compressive phase 1 reduces its thermal sensitivity. Finally, all tests heated with "UR" denoted, as expected, low thermal expansion and no influence of this phenomenon on their overall stress-displacement responses.

Finally, Figure 26 illustrates the crack evolution during the heating cases (i) and (ii) of the test previously subjected to a pre-compression of -1.125 mm during step-1.

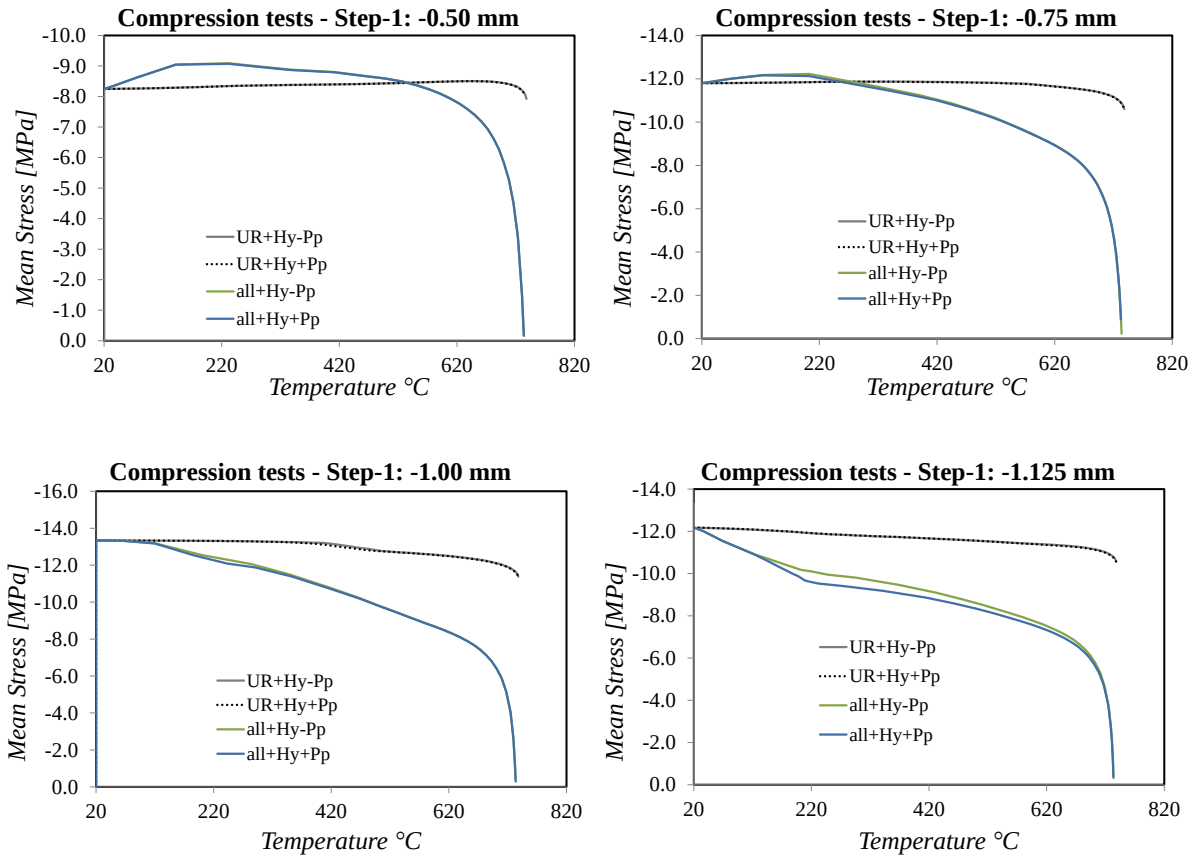

612

613

614 *Figure 25: Compressive stress-temperature response under fours pre-compression configurations*

615 *(step-1) and four boundary step-2 conditions.*

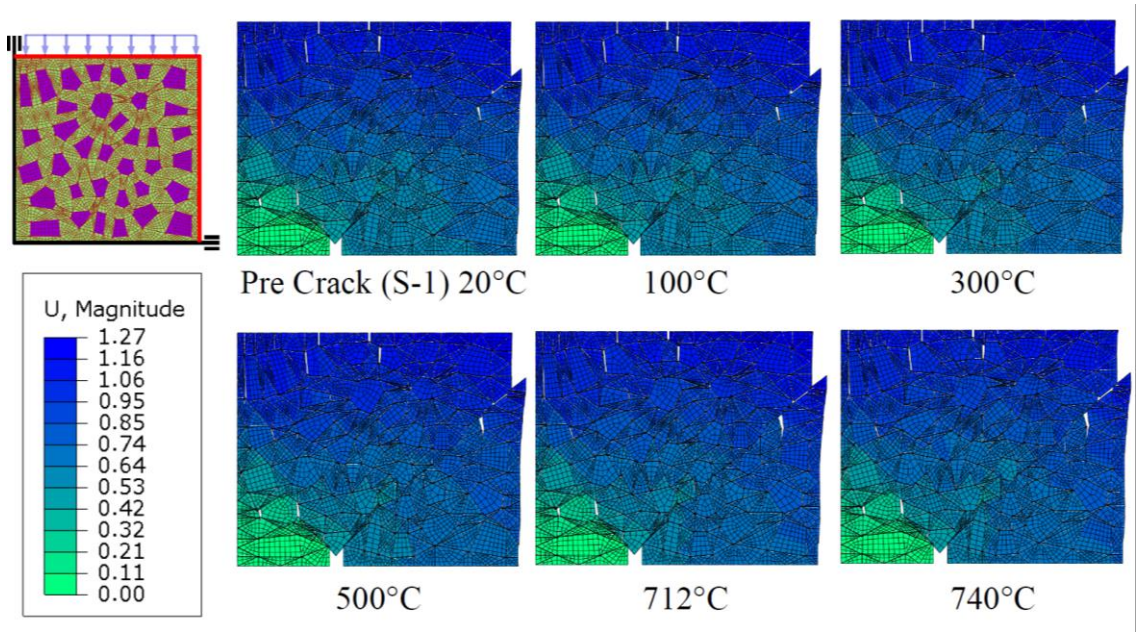

616

617 (a)

618

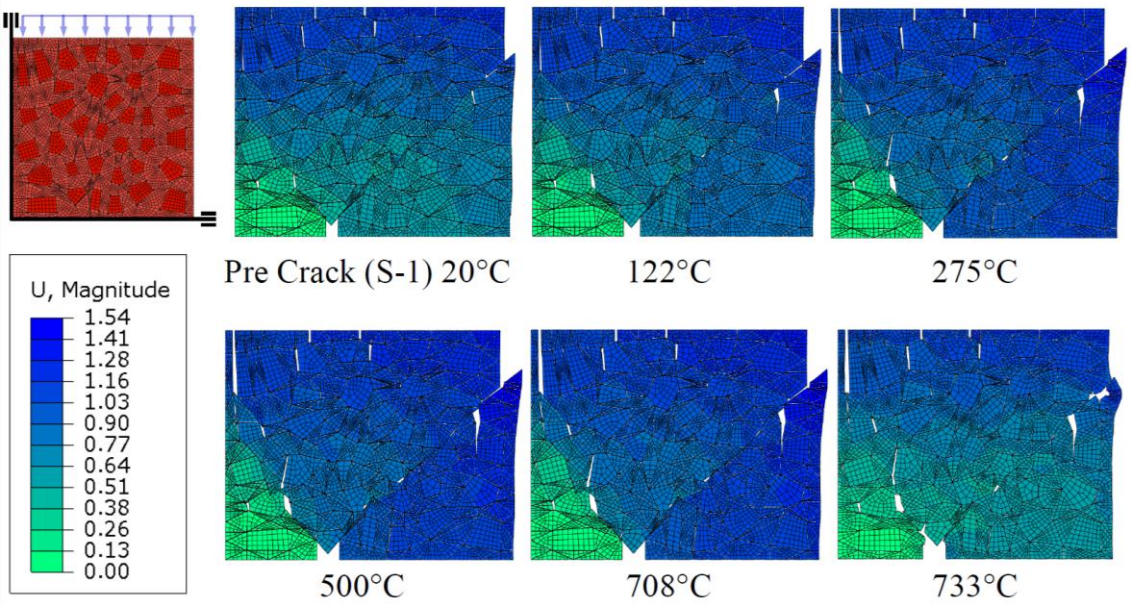

(b)

Figure 26: Crack pattern in a specimen subjected to pre-compression (step-1) of -1,125 mm: (a) UR+Hy+Pp and (b) all+Hy+Pp (deformation scale factor ×10).

The results presented in Figures 25 to 27 show the soundness and capability of the proposed interface model and numerical tools to analyze failure behavior of concrete components under coupled thermo-mechanical actions. They provide a simple and effective procedure for evaluating and, moreover, understanding the temperature and pore-pressure effects on concrete degradation and failure behavior without the need to explicitly model the hydraulic flux and vapor migration effects in concrete when subjected to high temperature.

4.5.3. Concluding remarks of mesoscopic thermo-mechanical tests

The results in the above Sections 4.5.1 and 4.5.2 aimed at demonstrating the phenomenological capabilities of the interface model to reproduce failure processes of concrete under combined mechanical, thermal and pore-pressure effects. Experimental studies, dealing with this kind of boundary conditions and complex actions are currently not available in the literature to properly verify the numerical-to-experimental soundness of the proposed mesoscopic thermo-mechanical

simulations. In spite of this, the included results clearly demonstrate that the proposed non-linear interface model formulation is able to provide realistic results and to reproduce the influence of the pore-pressure, de-hydration rules, strains induced by high temperature and the mechanical action on the overall composite mechanical response.

5. CONCLUSIONS

This paper proposed a mesoscopic approach based on non-linear thermoplastic and interfaces for modeling the failure response of porous cohesive-frictional composites induced by thermal damage due to the exposure to high temperature fields.

Particularly, the following main findings are proposed and discussed in this paper:

- A novel coupled pore-pressure based thermo-mechanical interface model for concrete, under the effects of intensive heating, has been proposed.
- The interface proposal accounts for the damage induced by the temperature dependent pore-pressure through a simple but very effective procedure;
- In this sense, the proposed interface constitutive equations are defined in terms of the "effective stresses" and pore-pressure, thereby, the influence of the last one on the normal total interface stress is taken into account;
- The strongly coupled multi-physics of the considered problem and the non-linear response of the interface model is activated not only by kinematic discontinuities but also by thermal and hydraulic processes;
- The proposed interface model allowed accurate and realistic mesoscopic simulations of concrete cracking when exposed to high temperature;
- Additionally, this discontinuous formulation was able to capture the strong thermal sensitivity of concrete's mechanical response, in the range from room to high temperature.

The numerical predictions of the proposed interface model for coupled thermo-mechanical failure analysis were evaluated under different temperature, mechanical conditions and pore-pressure effects considering a huge variability of test cases and boundary conditions. It is important to remark that the main purpose and intention of this investigation was to present a novel and effective model formulation and methodology to consider the pore-pressure concentration effects on concrete failure mechanism, when subjected to the combined action of temperature diffusion and mechanical

665 loading. The results demonstrated the phenomenological capability of the interface model to
666 reproduce the above mentioned coupled thermo-mechanical processes in concrete. It should be said
667 however that, so far, the experimental analysis of concrete specimens subjected to those complex
668 combined thermo-mechanical actions, under non-uniform temperature and non-residual state, is an
669 ongoing subject and, therefore, the available data in the literature are still insufficient. The
670 comparison between numerical predictions with experimental results of concrete elements subjected
671 to such combined mechanical and thermal actions (not residual tests) will be the main focus of a
672 subsequent paper.
673 As a final comment, it is worth to mention that the proposed interface model can also be employed
674 in multiscale studies with some of the involved physical, mechanical and thermal variables being
675 evaluated through homogenization procedures. Moreover, the proposed temperature-dependent
676 interface model can be easily extended for 3D thermo-mechanical failure analyses of concrete
677 components subjected to thermomechanical actions. These two latter represent straightforward
678 applications of the model and will be the scope of future works in this research line.
679

ACKNOWLEDGEMENTS

The Alexander von Humboldt-Foundation is acknowledged for funding the research position of Dr. A. Caggiano at the Institute of Construction and Building Materials at TU-Darmstadt under the research grant ITA-1185040-HFST-(2CENENRGY project). Moreover, the support to networking activities provided by the SUPERCONCRETE Project (H2020-MSCA-RISE-2014 n 645704; http://www.superconcreteh2020.unisa.it/) funded by the European Union is also gratefully acknowledged.

REFERENCES

[1] Ripani, M., Etse, G., Vrech, S. and Mroginski, J. 2014. Thermodynamic gradient-based poroplastic theory for concrete under high temperatures, Int J Plasticity, 61:157-177.

[2] Kose, M. M., Temiz, H., & Binici, H. 2006. Effects of fire on precast members: A case study. Engineering Failure Analysis, 13(8):1191-1201.

[3] Gao, W.Y., Dai, J.G., Teng, J.G. and Chen, G.M. 2013. Finite element modeling of reinforced concrete beams exposed to fire. Eng. Struct. 52:488-501.

[4] Gernay, T. and Franssen, J.M. 2015. A plastic-damage model for concrete in fire: Applications in structural fire engineering. Fire Safety J., 71:268-278.

[5] Gawin, D., Pesavento, F. and Schrefler, B. 2003. Modelling of hygro-thermal behaviour of concrete at high temperature with thermo-chemical and mechanical material degradation, Comp Meth App Mech Engng, 192: 1731-1771.

[6] Bahr, O., Schaumann, P., Bollen, B. and Bracke, J. 2013. Young's modulus and Poisson's ratio of concrete at high temperatures: Exp. investigations, Mat and Design, 45:421-429.

[7] Kizilkanat, A.B., Yuzer, N. and Kabay, N. 2013. Thermo-physical properties of concrete exposed to high temperature, Cons Build Materials, 45: 157-161.

[8] Tanyildizi, H. and Coskun, A. 2008. The effect of high temperature on compressive strength and splitting tensile strength of structural lightweight concrete containing fly ash, Construct Building Materials, 22:2269-2275.

[9] Phan, L.T. and Carino, N.J. 2002. Effects of test conditions and mixture proportions on behavior of high-strength concrete exposed to high temperatures, ACI Material J, 99:54-66.

[10] Lee, J., Xi, Y. And Willam, K. 2008. Properties of concrete after high-temperature heating and cooling. ACI Mater. J. 105:334-341.

[11] Zhang, B. and Bicanic, N. 2002. Residual fracture toughness of normal- and high-strength gravel concrete after heating to 600C. ACI Mat. J. 99:217-226.

[12] Zhang, B. 2011. Effects of moisture evaporation (weight loss) on fracture properties of high performance concrete subjected to high temperatures. Fire Safety J. 46:543-549.

[13] Janotka, I. and Bagel, L. 2002. Pore structures, permeabilities, and compressive strengths of concrete at temperatures up to 800 C. ACI Mater. J. 100:196-200.

[14] Harmathy, T.Z. 1970. Thermal Properties of Concrete at Elevated Temperature, J. of Material 5:47-74.

[15] Kalifa, P. and Menneteau, F.D. and Quenard, D. 2000. Spalling and porepressure in HPC at high temperature, Cem Concrete Research 1:1915-1927.

[16] Kalifa, P., Chene, G. and Galle, C. 2001. High-temperature behavior of HPC with polypropylene fibres: From spalling to microstructure ,Cement Concrete Research 31(10):1487-1499.

[17] Bazant, Z.P. 1997. Analysis of pore pressure, thermal stresses and fracture in rapidly heated concrete, Int. Workshop on Fire Performance of High Strength Concrete 13-14, CD-ROM.

[18] Gawin, D. and Schrefler, B.A. 1996. Thermo-hydro-mechanical analysis of partially saturated porous materials, Eng. Computations 13(7):113-143.

[19] Hager I. 2013. Behaviour of cement concrete at high temperature. Bull. Pol. Ac.: Tech. 61(1):1-10.

[20] Schrefler, B.A., Gawin, D., Majorana, C.E., and Pesavento, F. 2001. FE analysis of thermo-hydro mechanical behaviour of concrete at high temperature. Comput Mech - New Front for new millennium S. pp. 827-836.

[21] Caggiano, A. and Etse, G. 2015. Coupled thermo–mechanical interface model for concrete failure analysis under high temperature. Computer Methods in App Mech & Engineering 289:498-516.

[22] Klein R. Concrete and abstract Voronoi diagrams. Lecture Notes in Computer Science, Springer-Verlag, Berlin, 1989.

[23] Lopez CM, Carol I, Aguado A. Meso-structural study of concrete fracture using interface elements. I: numerical model and tensile behavior. Mater Struct 2008;41(3):583–99.

[24] Lopez CM, Carol I, Aguado A. Meso-structural study of concrete fracture using interface elements. II: compression, biaxial and brazilian test. Mater Struct 2008;41(3):601–20.

[25] Chang, Y. F., Chen, Y. H., Sheu, M. S. and Yao, G.C. 2006. Residual stress-strain relationship for concrete after exposure to high temperatures. Cement Concrete Res. 36:1999-2005.

[26] Guo, Z. and Shi, X. 2011. Experiment and Calculation of Reinforced Concrete at Elevated Temperatures, 1st edition. Ed. Butterworth-H. Waltham, USA.

[27] Segura, J.M. and Carol I. 2008. Coupled HM analysis using zero-thickness interface elements with double nodes. Part I: Theoretical model, Int. J. Numer. Anal. Meth. Geomech. 32:2083-2101.

[28] Majorana, C. E., Salomoni, V., & Schrefler, B. A. (1998). Hygrothermal and mechanical model of concrete at high temperature. Materials and structures, 31(6), 378-386.

[29] Pereira, F., Pistol, K., Korzen, M., Weise, F., Pimienta, P., Carré, H. and Huismann, S. 2011. Monitoring of fire damage processes in concrete by pore pressure and acoustic emission measurements. 2nd international Rilem workshop on concrete spalling due to fire exposure, Delft, The Nederlands (pp. 5-7).

[30] Willam, K., Rhee, I., Shing, B. 2004. Interface damage model for thermo-mechanical degradation of heterogeneous materials, Computer Methods in Applied Mechanics and Engineering 193, 3327 - 3350.

[31] Said Schicchi D., Caggiano A., Benito S. and Hoffmann F. Mesoscale fracture of a bearing steel: a discrete crack approach on static and quenching problems. Theoretical and Applied Fracture Mechanics, 2017; 90:154-164

[32] Caggiano A, Said Schicchi D, A thermo-mechanical interface model for simulating the bond behaviour of FRP strips glued to concrete substrates exposed to elevated temperature, Eng Struct, 2015, 83:243-251.

[33] Bamonte, P., & Felicetti, R. (2007). On the tensile behavior of thermally-damaged concrete. In Proceedings of the 6th International conference on Fracture Mechanics of Concrete and Concrete Structure-FraMCoS6 (Vol. 3, p. 8).

[34] EN 1992-1-2 2004. (English): Eurocode 2: Design of concrete structures - Part 1-2: General rules - Structural fire design.

[35] Gawin, D., Majorana,C.E. and Schrefler, B.A. 1999. Numerical analysis of hygro-thermic behaviour and damage of concrete at high temperature, Mech.Cohes.-Frict. Mater. 4:37-74.

[36] Gawin, D., Pesavento, F. and Schrefler, B.A. 2002. Simulation of damage–permeability coupling in hygro-thermo-mechanical analysis of concrete at high temperature, Commun. Numer. Methods Engrg. 18:113-119.

[37] Gawin, D., Pesavento, F. and Schrefler, B.A. 2004. Modelling of deformations of high strength concrete at elevated temperatures, Concr. Sci. Engrg./ Mater. Struct. 37(268):218-236.

[38] Khoury, G.A. 1995. Strain components of nuclear-reactor-type concretes during first heating cycle, Nucl. Engrg. Des. 156:313-321.

[39] Caballero, A., Willam, K. J., & Carol, I. (2008). Consistent tangent formulation for 3D interface modeling of cracking/fracture in quasi-brittle materials. Computer Methods in Applied Mechanics and Engineering, 197(33), 2804-2822.

[40] Pepe, M., Toledo Filho, R. D., Koenders, E. A., & Martinelli, E. (2016). A novel mix design methodology for recycled aggregate concrete. Construction and Building Materials, 122, 362-372.

[41] Pepe, M. (2015). A conceptual model for designing recycled aggregate concrete for structural applications. Springer.

[42] Lopez CM (1999) Microstructural analysis of concrete fracture using interface elements. Application to various concretes (In Spanish). Doctoral Thesis. Universitat Politecnica de Catalunya. ETSECCCP-UPC, E-08034 Barcelona, Spain.

[43] Caballero, A., Carol, I., & López, C. M. (2007). 3D meso-mechanical analysis of concrete specimens under biaxial loading. Fatigue & Fracture of Engineering Materials & Structures, 30(9), 877-886.

[44] Idiart, A. E., López, C. M., & Carol, I. (2011). Modeling of drying shrinkage of concrete specimens at the meso-level. Materials and structures, 44(2), 415-435.